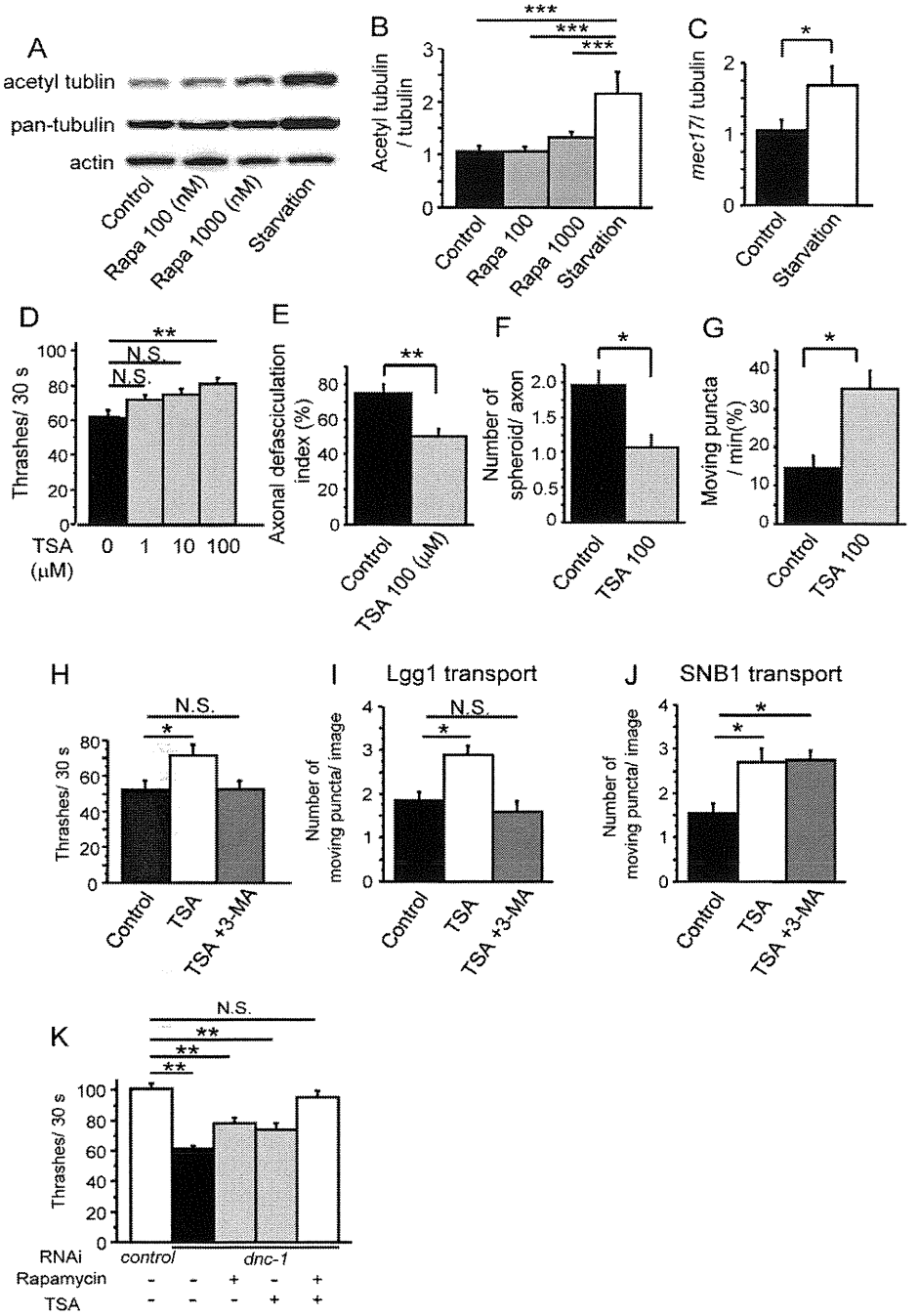

Figure 11. The effects of tubulin acetylation on the transport of autophagosome and neurodegeneration in the *dnc-1(RNAi)* worms. (*A, B*) Immunoblots of primary cultured cells using antibodies against acetylated tubulin, pan-tubulin, and actin (n = 5). (*C*) The mRNA levels of *mec17* measured by real-time RT-PCR. The data shown are ratios to the mRNA levels of *tba1*, the gene encoding alpha-tubulin. (*D*) Effect of trichostatin A (TSA) on the locomotor function of the *dnc-1(RNAi)* worms (n = 35 for each group). (*E–G*) Effect of TSA (100 μM) on the axonal degeneration of the *dnc-1(RNAi)* worms (*E, F*) and on autophagosome mobility (*G*) (n = 15 for each group). (*H*) The inhibition of autophagy by 3-MA (10 mM) negates the effect of TSA treatment on the motor function of the *dnc-1(RNAi)* worms (n = 35 for each group). (*I, J*) The number of moving puncta (*I*, Lgg1; *J*, SNB1) was counted using kymographs derived from *in vivo* time-lapse images (n = 20 images for each analysis). Treatment with 3-MA negates the effect of TSA treatment on the transport of Lgg1 (*I*), but not the transport of SNB1 (*J*). (*K*) Combination therapy of rapamycin (100 μM) and TSA (100 μM) has synergistic effects on the locomotive functions of the *dnc-1(RNAi)* worms (n = 35 for each group). Statistical analyses were performed by one-way ANOVA followed by the Bonferroni/Dunn post hoc test for (*B*), Dunnett's post hoc test (*D, H–K*), and Student's t test (*C, E–G*) (*p<0.05, **p<0.001, and ***p<0.0001). The error bars are S.E.M.
doi:10.1371/journal.pone.0054511.g011

(Fig. 3*D, E*). The thrashing speed of the *control(RNAi)* worms was slightly decreased compared with the wild-type worms, possibly due to the toxicity of GFP, as previously reported [32] (Fig. 3*E*). Although the toxicity of GFP was much less than that of *dnc-1* knockdown and not detectable in the bending assay, to exclude any effects of the fluorescent protein on our analysis, we compared

the *dnc-1(RNAi)* worms with the *control(RNAi)* worms, both of which express GFP at similar levels, in all experiments. We also performed a video capture analysis to visualize the movement trace of each worm and measure its average speed (Fig. 3*F*, *G*). The movement speed was dramatically decreased in the *dnc-1(RNAi)* worms compared with the *control(RNAi)* worms at an early adult stage.

Axonal degeneration is the early sign of neurodegeneration in the *dnc-1(RNAi)* worms

We then examined the morphological changes in the *dnc-1(RNAi)* worms using fluorescent microscopy. In normal worms, the ventral nerve cords were tightly fasciculated and the motor-neuron cell bodies (white asterisks in Fig. 4*A*) were round or ovoid. (Fig. 4*B*, *C*). By contrast, we found irregular shapes and defasciculation of the ventral nerve cord as well as axonal swellings, or spheroids, in the *dnc-1(RNAi)* worms at an early stage (Fig. 4*D*). At this early stage (4 days old), the cell bodies in the *dnc-1(RNAi)* worms seemed normal judging from their shape and structure (Fig. 4*D*). However, at a later adult stage (7 days old), axonal degeneration was exacerbated and morphological changes were also detected in the cell bodies (Fig. 4*E*). Axonal changes were occasionally observed in the *control(RNAi)* worms with aging, but they were less frequent and not as severe as in the *dnc-1(RNAi)* worms (Fig. 4*C*). Semi-quantification of the axonal and cell body changes showed that the axonal abnormalities were observed at day 4 and cell body deformation occurred at a later stage (Fig. 4*F*). Although some neurons exhibited an abnormal cell body shape at day 4, this change was only observed in the worms with axonal defasciculation (Fig. 4*G*), indicating that axonal degeneration occurs prior to cell body degeneration. Moreover, we also found that the severity of axonal defasciculation (i.e., the axonal defasciculation index) was correlated with locomotor dysfunction in the *dnc-1(RNAi)* worms (Fig. 4*H*). To clarify the time-course of the neuronal changes due to *dnc-1* depletion, we also examined the morphological change during the developmental stage. The acr2p::shRNA::GFP is not detectable before larval stage L1 (Fig. S1*A–C*). Furthermore, even after GFP is expressed, there was no alteration in morphology or motor phenotype during the larval stage (from L1 to L4, post natal days 1 and 2) (Fig. S1*C–E*). It was only after the worms became adult that the axonal degeneration and motor deficit appeared. Taken together, these findings suggest that the depletion of *dnc-1* induces the degeneration, rather than developmental defects, of motor neurons in *C. elegans*.

Further analysis via electron microscopy confirmed the axonal degeneration in the *dnc-1(RNAi)* worms (Fig. 5*C–F*). In the early degenerative stage, *dnc-1(RNAi)* worms first exhibited whorl like inclusions in axons with only a few morphological changes in their cell bodies (Fig. 5*C*, *D*) compared with *control(RNAi)* worms (Fig. 5*A*, *B*). In the later degenerative stage, strikingly abundant whorl-like inclusions and vacuoles, corresponding to degeneration and swelling of axons [21], were observed in axons and cell bodies (Fig. 5*E*, *F*).

Axonal transport defect in the *dnc-1(RNAi)* worms

Abnormalities in the localization and accumulation of synaptic vesicles were reported in a *C. elegans* model showing a defect in axonal transport [20]. To determine whether our *dnc-1(RNAi)* model exhibited defects in axonal transport, we used a fluorescently tagged synaptic vesicle marker composed of the *C. elegans* VAMP2/synaptobrevin protein fused to DsRed (SNB-1::DsRed), and examined the distribution of the dorsally located red puncta (Fig. 6*A*). In the dorsal nerve cord (the axons of the ventral motor neurons) of the *control(RNAi)* worms, SNB-1::DsRed puncta were regularly spaced, whereas the *dnc-1(RNAi)* worms exhibited a discontinuous and irregular distribution of the marker, including occasional clumps that may represent the accumulation of cargo proteins (Fig. 6*B*). Histograms of the distances between neighboring SNB-1 puncta displayed a broader curve in the *dnc-1(RNAi)* worms than in the *control(RNAi)* worms, suggesting some defect in axonal transport caused by the knockdown of *dnc-1* (Fig. 6*C*, *D*).

To demonstrate direct evidence of a defect in axonal transport in our transgenic worms, we monitored the movement of SNB-1 puncta by acquiring a series of time-lapse images. The resulting kymographs showed that puncta in the *dnc-1* KD worms were markedly static compared with those in the controls, confirming the disruption of axonal transport following the reduction of *dnc-1* in *C. elegans* (Fig. 6*E*, *F*, Movies S1, S2). To quantify the movement of SNB-1, we analyzed 20 kymographs from each strain. While there was no significant difference in the number of SNB-1 puncta between the *control(RNAi)* and *dnc-1(RNAi)* worms (Fig. 6*G*), the number of moving puncta (moving more than 2 μm) (Fig. 6*H*) and the ratio of moving puncta to total puncta (Fig. 6*I*) were significantly decreased in the *dnc-1(RNAi)* worms compared to the *control(RNAi)* worms ($p = 0.028$ and $p = 0.014$, respectively). The velocity of SNB-1 transport in the *dnc-1(RNAi)* worms was significantly lower than in the *control(RNAi)* worms ($p<0.0001$, Fig. 6*J*).

Impaired transport and accumulation of autophagosomes in the *dnc-1(RNAi)* worms

We next investigated the effects of *dnc-1* depletion on autophagy in *C. elegans*. Autophagosomes are cargo that moves bidirectionally along microtubules, powered by the kinesin family of motor proteins and dynein/dynactin complexes [11,12]. Altered autophagy has been observed in several neurodegenerative models, including the mutant *DCTN1* mouse model [9,16,33,34]. However, little is known about the relationship between the decreased levels of dynactin 1 and the alteration of autophagy. To clarify the effect of quantitative loss of DNC-1/dynactin 1 in the transport of autophagosomes, we performed live-cell imaging analyses of autophagosome transport in the axons of primary cultured motor neurons from the *dnc-1(RNAi)* and *control(RNAi)* worms that co-expressed DsRed-tagged Lgg1/ATG8, which is associated with the autophagic membrane, in ventral motor neurons under the control of the *acr2* promoter (Mizushima et al. [35]. This marker of autophagosomes is expressed diffusely in the ventral motor neurons (Fig. S2*A*) and forms distinct puncta when autophagosomes are formed (Fig. S2*B*) [36]. In the *control(RNAi)* neurons, the fluorescent Lgg1 vesicles moved toward and away from the cell body, suggesting that these vesicles are powered by anterograde and retrograde motors (Fig. 7*A*, Movie S3). By contrast, in the *dnc-1(RNAi)* worms, the autophagosomes were easily trapped where the axon was tight or curved, or at spheroids (Fig. 7*B*, Movie S4). This phenomenon was followed by the accumulation of autophagosomes distal to the trapped sites. Histograms showing the distribution of the velocity and distance of autophagosome movement demonstrated a significant loss of fast- and long-moving vesicles in the *dnc-1(RNAi)* cells compared with the *control(RNAi)* cells (Fig. 7*C*, *D*). The mean velocity and movement distance (run-length) were significantly decreased in the anterograde and retrograde directions in the *dnc-1(RNAi)* neurons ($p<0.0001$, $=0.0001$; velocity of anterograde, retrograde movements, respectively, and $p = 0.0045$, <0.0001; run-length of anterograde, retrograde movements, respectively) (Fig. 7*E*, *F*).

Next, we performed kymograph analysis of Lgg1::DsRed using *in vivo* time-lapse images (Fig. 8*A*, *B*, Movie S5, S6). Although the total number of Lgg1 puncta was significantly increased

($p<0.0001$) (Fig. 8*C*), the number (Fig. 8*D*) and the ratio of moving puncta (Fig. 8*E*) were significantly decreased in the *dnc-1(RNAi)* worms compared with the *control(RNAi)* worms ($p = 0.013$ and $p<0.0001$, respectively). The velocity of Lgg1 movement was also significantly decreased in the *dnc-1(RNAi)* worms ($p<0.0001$) (Fig. 8*F*). These results indicated that the *dnc-1* depletion resulted in the accumulation of untransported autophagosomes in the motor neurons.

We then investigated whether the accumulation of autophagosomes is related to the motor neuron degeneration. In the ventral nerve cord of the *dnc-1(RNAi)* worms, the number of Lgg1 puncta was significantly increased in comparison with the *control(RNAi)* worms ($p = 0.019$) (Fig. 8*G*), and the accumulation of autophagosomes was correlated with the axonal defasciculation index and locomotor function (Fig. 8*H*, *I*). We also explored the localization of Lgg1::DsRed in the distal ascending axon and observed Lgg1::DsRed accumulation in axonal spheroids (Fig. S2*C*), which is consistent with a previous report showing the abnormal accumulation of disorganized organelles and autophagosomes in axonal spheroids [37]. Electron microscopy showed that the accumulation of vesicular structures, including autophagosome-like vesicles and mitochondria, was observed in the proximal axons or cytoplasm of the *dnc-1(RNAi)* worms, although such accumulations were detected rarely in the axons of the *control(RNAi)* neurons (Fig. 8*J–L*).

We then treated the *control(RNAi)* worms with 3-MA, which inhibits the formation of autophagosomes (Fig. 9*A*). These worms showed the locomotory defects and axonal degeneration observed in the *dnc-1(RNAi)* worms, suggesting that the disrupted autophagy system is sufficient to cause the motor neuronal degeneration in this model (Fig. 9*B–E*). On the other hand, when we treated the *dnc-1(RNAi)* worms with 3-MA, worms did not exhibit a substantial change in the motor function or in the axonal integrity (Fig. 9*F–H*).

Starvation dramatically attenuates the motor deficits in the *dnc-1(RNAi)* worms by facilitating the axonal transport of autophagosomes

Autophagy is known to be activated by rapamycin, a specific inhibitor of the mTOR pathway [38]. Starvation is also a strong activator of autophagy; however, it also has other effects, e.g., activation of the mitogen-activated protein kinase (MAPK) pathway [39], stimulation of tubulin acetylation [40], and induction of sirtuin [41]. Both treatments have been used widely in many species, e.g., *Drosophila*, mouse, and *C. elegans*, to activate autophagy [42–44].

To study the effects of autophagy activators on axonal degeneration in *C. elegans*, we treated the *control(RNAi)* and *dnc-1(RNAi)* worms with rapamycin or starved them by food restriction, and investigated the changes in motor function via the liquid thrashing assay. Rapamycin and starvation are known to extend lifespan of *C. elegans* [42,45]. In the present study, we found that neither rapamycin nor starvation significantly altered the motor function of the *control(RNAi)* worms (Fig. 10*A*). In the *dnc-1(RNAi)* worms, rapamycin ameliorated the thrashing activity in a dose-dependent manner, although it showed only a limited effect even at the most effective dose (Fig. 10*A*). In contrast, starvation completely ameliorated the motor dysfunction of the *dnc-1(RNAi)* worms without affecting the efficiency of *dnc-1* knockdown (Fig. 10*A*, Fig. S3*A–C*). The formation of axonal spheroids was also significantly suppressed by starvation ($p = 0.001$) (Fig. 10*B*, *C*). Given the differential effects of rapamycin and starvation, we hypothesized that starvation not only increases the formation of autophagosomes but also increases their mobility in axons. Indeed, the frequency of autophagosome movement was increased by food restriction (Fig. 10*D*). To further confirm this hypothesis, we cultured primary motor neurons from the *dnc-1(RNAi)* worms in serum-depleted medium, and quantified the mobility of autophagosomes by monitoring the movement of DsRed-tagged Lgg1 in axons. As we expected, starvation significantly increased the speed and run-length of moving Lgg1 puncta, especially the retrograde run-length, in the *dnc-1(RNAi)* worms ($p<0.0001$) (Fig. 10*E*, *F*). Conversely, neurons treated with rapamycin showed no detectable change in the transport of autophagosomes (Fig. 10*E*, *F*). Histograms showing the distribution of the velocity and distance of autophagosome movement also demonstrated a significant increase of fast- and long-moving vesicles in the starved cells, especially in retrograde transport (Fig. 10*G*, *H*). For example, the percentage of vesicles that moved more than 8 μm retrogradely increased from 6.9% (*dnc-1(RNAi)* control) to 27.0% (*dnc-1(RNAi)* starvation), whereas the change was only from 12.7% to 19.7% in the anterograde direction (Fig. 10*H*).

Finally, we investigated how starvation stimulates the axonal transport of autophagosomes and assessed whether drugs that mimic the molecular mechanisms of starvation enhanced its effect. The acetylation of tubulin is known to stabilize microtubules and activate axonal transport by the subsequent recruitment of the molecular motors kinesin-1 and dynein/dynactin to microtubules [46,47]. Therefore, we assessed the acetylation state of alpha-tubulin in our cultured cell assay. Starvation increased the levels of acetylated tubulin, but this effect was not detected in cells treated with rapamycin (Fig. 11*A*, *B*). Moreover, real-time quantitative PCR demonstrated that starvation, but not rapamycin, significantly increased the mRNA levels of *mec-17*, an enzyme that acetylates tubulin in *C. elegans* [48] (Fig. 11*C*). Taken together, our results suggest the possibility that starvation mitigated axonal degeneration by activating autophagy and promoting the axonal transport of autophagosomes via the acetylation of tubulin in the *dnc-1(RNAi)* worms. To test this hypothesis, we examined the effects of TSA, an HDAC inhibitor that facilitates tubulin acetylation, on the phenotypes of the *dnc-1(RNAi)* worms. Although treatment with TSA did not exhibit substantial effects on the phenotype of the *control(RNAi)* worms (Fig. S4*A–C*), this treatment showed a significant effect on the locomotory function of the *dnc-1(RNAi)* worms in a dose-dependent manner, and attenuated the axonal degeneration without alteration of *dnc-1* knockdown efficiency (Fig. 11*D–F*, Fig. S3*A*, *B*, *and D*). As expected, TSA increased the mobility of autophagosomes (Fig. 11*G*). Interestingly, treatment with 3-MA dampened the effect of TSA on locomotion (Fig. 11*H*). On the contrary, the worms treated with both TSA and 3-MA showed decreased transport of autophagosomes without defects in the transport of synaptobrevin (Fig. 11*I*, *J*). Furthermore, we also examined the effect of combination therapy with rapamycin and TSA. Although treatment with rapamycin or TSA alone had limited effects in comparison with *control(RNAi)* worms, the combination of rapamycin and TSA had greater effects such that locomotion was restored in the worms treated with these two drugs to the levels observed in the *control(RNAi)* worms (Fig. 11*K*).

Discussion

In the present study, we generated a novel *C. elegans* model that mimics the down-regulation of dynactin 1 observed in the motor neurons of SALS patients. Using this model, we investigated whether the quantitative loss of DNC-1/dynactin 1 causes motor neuron degeneration. Our results showed that the knockdown of *dnc-1* caused progressive motor deficits in *C. elegans*, and the

pathological changes observed in this model shared several features with those seen in SALS patients, e.g., the axonal accumulation of membranous structures, such as mitochondria and autophagosomes, and motor neuron degeneration characterized by axonal degeneration including axonal spheroids. We also observed the disrupted transport of autophagosomes in the degenerated motor neurons of this model. Interestingly, our model exhibited adult-onset motor neuron degeneration even though the *shRNA::gfp* had already expressed in the larval stage. Given that the patients carrying mutant *DCTN1* and SALS patients exhibit an adult-onset motor neuron degeneration, it is possible that developing motor neurons are resistant to the disruption of DNC-1/dynactin 1. However, differentiated motor neurons may be vulnerable to the detrimental effects of dynactin 1 depletion, since they require more efficient transport system to maintain axonal homeostasis than developing neurons. Together, these findings indicate that this *dnc-1*-KD *C. elegans* model is a powerful tool for understanding the relationship between the disrupted transport of autophagosomes, neurodegeneration, and motor phenotype.

The mechanism of autophagosome accumulation in motor neurons harboring a motor protein abnormality was shown directly by our analysis of autophagosomal transport; namely, the knockdown of *dnc-1* decreased the transport of autophagosomes and shortened their run-length. Physiological cargoes typically use multiple motors, and their run-lengths are correlated with the number of coordinated motor proteins [49]. Our results showed that the knockdown of *dnc-1* reduced the speed and distance of retrograde transport by approximately half. These results are consistent with previous *in vitro* studies of dynein showing that the run-length of retrograde motor complexes is reduced by approximately half in cells lacking dynactin 1 [49,50]. Our data indicated that the knockdown of *dnc-1* also affected the anterograde transport of autophagosomes, which is consistent with previous reports showing that a defect in retrograde transport led to dysregulated movements in both directions [51,52].

The relationship between the decreased DNC-1/dynactin 1 levels, the increased number of autophagosomes, and axonal degeneration was confirmed by our observations that the *dnc-1(RNAi)* worms showed an abnormal accumulation of autophagosomes and that their locomotory defects and axonal degeneration were correlated with the accumulation of autophagosomes. Furthermore, the *control(RNAi)* worms treated with 3-MA, an inhibitor of autophagy, showed the same phenotype as the *dnc-1(RNAi)* worms, including defective locomotory function and degenerated axons. Taken together, our findings in the *dnc-1(RNAi) C. elegans* model provide direct evidence that the lack of DNC-1/dynactin 1 in dynein/dynactin motor complexes leads to slow, short-distance movements of autophagosomes, followed by their axonal accumulation, and neurodegeneration.

It is clinically important to determine whether the activation of autophagy could be an effective therapeutic strategy against neurodegenerative diseases, especially when the transport of autophagosomes is disrupted. In previous studies, the effects of rapamycin, which induces autophagosome formation [9], against models of neurodegeneration were controversial [53–55]. In the present study, rapamycin only slightly ameliorated the motor dysfunction of the *dnc-1(RNAi)* worms, although its effects were substantially enhanced by the addition of TSA which enhances the acetylation of tubulin. Given that tubulin acetylation was shown to stimulate axonal transport [47], our results suggest that combination therapy with rapamycin and TSA, attenuated the neurodegeneration and locomotory dysfunction of this model by facilitating the formation and axonal transport of autophagosomes.

Although it is still possible that the disrupted transport of other organelles such as mitochondria are also involved in the pathogenesis of motor neuron degeneration in the *dnc-1(RNAi)* worms, the observation that 3-MA, an inhibitor of autophagy, almost completely abrogated the benefit effects of TSA suggests a substantial role for autophagosomal transport in the functional maintenance of motor neurons. This view is further supported by the fact that the worms treated by both TSA and 3-MA showed the decreased transport of autophagosomes without defects in the transport of synaptobrevin.

In conclusion, we found that decreased levels of dynactin 1 in motor neurons induce neurodegeneration at least partially via the disruption of the axonal transport of autophagosomes. The therapeutic strategy we examined in this study could be expanded to other neurodegenerative disorders, since the accumulation of autophagosomes and disrupted axonal transport are common features of many neurodegenerative diseases. Future study is needed to explore the effectiveness and safety of the treatments that stimulate the transport of autophagosomes in the mammalian central nervous system.

Supporting Information

Figure S1 Expression pattern of *shRNA*::GFP and morphology of ventral motor neurons during embryonic and larval stage. (*A, B*) Representative confocal micro scopic image of *shRNA*::GFP expression during embryonic stages. GFP was not observed in the eggs even after delivery (asterisks in *A, B*). (*C–E*) GFP expression were observed in the ventral motor neurons (black arrows in *C*) from L1 (larval 1) stage of the worms. The ventral nerve axons (white arrows in *D, E*) did not exhibit abnormal changes such as axonal swellings or defasciculations during L1-4. Scale bars = 20 μm (*A–C*), 100 μm (low magnification image in *D, E*), or 50 μm (high magnification in *D, E*).
(TIF)

Figure S2 Expression pattern of the Lgg1::DsRed in the *control(RNAi)* worm and the *dnc-1(RNAi)* worm. (*A, B*) Representative fluorescent microscopic views of the Lgg1::DsRed in the ventral nerve cord of *control(RNAi)* worms (*A*) and *dnc-1(RNAi)* worms (*B*). The Lgg1 puncta (asteriscs in *B*) was abundant in the *dnc-1(RNAi)* worms (*B*). (*C*) Co-localization of DsRed and GFP fluorescence in the axonal spheroids (arrows) indicating that the autophagosomes (asteriscs) were accumulated in the axonal spheroids in the *dnc-1(RNAi)* worms. Scale bar = 10 μm (*A–C*).
(TIF)

Figure S3 Pharmacological treatment or starvation did not alter the efficiency of the *dnc-1* knock-down. (*A–D*) The representative image of GFP and *in situ* hybridization against *dnc-1* of ventral cholinergic motor neurons in the *conrol(RNAi)* (*A*) and *dnc-1(RNAi)* (*B*, no treatment; *C*, treated with starvation; *D*, treated with TSA). Scale bars = 10 μm.
(TIF)

Figure S4 Treatment with TSA did not alter the locomotor function or the axonal integrity of the *control(RNAi)* worms. (*A*) Effect of trichostatin A (TSA) on the locomotor function of the *control(RNAi)* worms (n = 35 for each group). (*B, C*) Effect of TSA (100 μM) on the axonal degeneration of the *dnc-1(RNAi)* worms (n = 15 for each group). Statistical analyses were performed using Student's t test.
(TIF)

Movie S1 Representative transport of SNB-1::DsRed puncta (red) in a ventral motor neurons from the control worm.
(MPEG)

Movie S2 Representative transport of SNB-1::DsRed puncta (red) in a ventral motor neurons from the *dnc-1* KD worm.
(MPEG)

Movie S3 Representative transport of Lgg1::DsRed puncta (red) in a primary motor neuron from the control worm.
(MPEG)

Movie S4 Representative transport of Lgg1::DsRed puncta (red) in a primary motor neuron from the *dnc-1* KD worm.
(MPEG)

Movie S5 Representatie transport of Lgg1::DsRed puncta (red) in a ventral motor neurons from the control worm.
(MPEG)

Movie S6 Representatie transport of Lgg1::DsRed puncta (red) in a ventral motor neurons from the *dnc-1* KD worm.
(MPEG)

Materials and Methods S1 Detailed materials and methods for *C. elegans* and human protocols.
(DOCX)

Author Contributions

Conceived and designed the experiments: KI MK FT IM GS. Performed the experiments: KI K. Kawai ZH YI YJ K. Kobayashi TK MW. Analyzed the data: KI K. Kawai MK. Contributed reagents/materials/analysis tools: TK K. Kobayashi IM. Wrote the paper: KI MK FT GS.

References

1. Klionsky DJ, Emr SD (2000) Autophagy as a regulated pathway of cellular degradation. Science 290: 1717–1721.
2. Hara T, Nakamura K, Matsui M, Yamamoto A, Nakahara Y, et al. (2006) Suppression of basal autophagy in neural cells causes neurodegenerative disease in mice. Nature 441: 885–889.
3. Komatsu M, Waguri S, Chiba T, Murata S, Iwata J, et al. (2006) Loss of autophagy in the central nervous system causes neurodegeneration in mice. Nature 441: 880–884.
4. Ravikumar B, Acevedo-Arozena A, Imarisio S, Berger Z, Vacher C, et al. (2005) Dynein mutations impair autophagic clearance of aggregate-prone proteins. Nat Genet 37: 771–776.
5. Komatsu M, Wang QJ, Holstein GR, Friedrich VL Jr., Iwata J, et al. (2007) Essential role for autophagy protein Atg7 in the maintenance of axonal homeostasis and the prevention of axonal degeneration. Proc Natl Acad Sci U S A 104: 14489–14494.
6. Anglade P, Vyas S, Javoy-Agid F, Herrero MT, Michel PP, et al. (1997) Apoptosis and autophagy in nigral neurons of patients with Parkinson's disease. Histol Histopathol 12: 25–31.
7. Sapp E, Schwarz C, Chase K, Bhide PG, Young AB, et al. (1997) Huntingtin localization in brains of normal and Huntington's disease patients. Ann Neurol 42: 604–612.
8. Sasaki S (2011) Autophagy in spinal cord motor neurons in sporadic amyotrophic lateral sclerosis. J Neuropathol Exp Neurol 70: 349–359.
9. Yu WH, Cuervo AM, Kumar A, Peterhoff CM, Schmidt SD, et al. (2005) Macroautophagy--a novel Beta-amyloid peptide-generating pathway activated in Alzheimer's disease. J Cell Biol 171: 87–98.
10. Li L, Zhang X, Le W (2008) Altered macroautophagy in the spinal cord of SOD1 mutant mice. Autophagy 4: 290–293.
11. Yang Y, Xu K, Koike T, Zheng X (2008) Transport of autophagosomes in neurites of PC12 cells during serum deprivation. Autophagy 4: 243–245.
12. Katsumata K, Nishiyama J, Inoue T, Mizushima N, Takeda J, et al. (2010) Dynein- and activity-dependent retrograde transport of autophagosomes in neuronal axons. Autophagy 6: 378–385.
13. Jiang YM, Yamamoto M, Tanaka F, Ishigaki S, Katsuno M, et al. (2007) Gene expressions specifically detected in motor neurons (dynactin 1, early growth response 3, acetyl-CoA transporter, death receptor 5, and cyclin C) differentially correlate to pathologic markers in sporadic amyotrophic lateral sclerosis. J Neuropathol Exp Neurol 66: 617–627.
14. Puls I, Jonnakuty C, LaMonte BH, Holzbaur EL, Tokito M, et al. (2003) Mutant dynactin in motor neuron disease. Nat Genet 33: 455–456.
15. Levy JR, Sumner CJ, Caviston JP, Tokito MK, Ranganathan S, et al. (2006) A motor neuron disease-associated mutation in p150Glued perturbs dynactin function and induces protein aggregation. J Cell Biol 172: 733–745.
16. Laird FM, Farah MH, Ackerley S, Hoke A, Maragakis N, et al. (2008) Motor neuron disease occurring in a mutant dynactin mouse model is characterized by defects in vesicular trafficking. J Neurosci 28: 1997–2005.
17. Katsuno M, Adachi H, Kume A, Li M, Nakagomi Y, et al. (2002) Testosterone reduction prevents phenotypic expression in a transgenic mouse model of spinal and bulbar muscular atrophy. Neuron 35: 843–854.
18. Brenner S (1974) The genetics of Caenorhabditis elegans. Genetics 77: 71–94.
19. Takada T, Iida K, Sasaki H, Taira M, Kimura H (2005) Expression of ADP-ribosylation factor (ARF)-like protein 6 during mouse embryonic development. Int J Dev Biol 49: 891–894.
20. Koushika SP, Schaefer AM, Vincent R, Willis JH, Bowerman B, et al. (2004) Mutations in Caenorhabditis elegans cytoplasmic dynein components reveal specificity of neuronal retrograde cargo. J Neurosci 24: 3907–3916.
21. Kraemer BC, Zhang B, Leverenz JB, Thomas JH, Trojanowski JQ, et al. (2003) Neurodegeneration and defective neurotransmission in a Caenorhabditis elegans model of tauopathy. Proc Natl Acad Sci U S A 100: 9980–9985.
22. Miyara A, Ohta A, Okochi Y, Tsukada Y, Kuhara A, et al. (2011) Novel and Conserved Protein Macoilin Is Required for Diverse Neuronal Functions in Caenorhabditis elegans. PLoS Genet 7: e1001384.
23. Lewis JA, Fleming JT (1995) Basic culture methods. Methods Cell Biol 48: 3–29.
24. Strange K, Christensen M, Morrison R (2007) Primary culture of Caenorhabditis elegans developing embryo cells for electrophysiological, cell biological and molecular studies. Nat Protoc 2: 1003–1012.
25. Stiernagle T (2006) Maintenance of C. elegans. WormBook: 1–11.
26. Paredez AR, Persson S, Ehrhardt DW, Somerville CR (2008) Genetic evidence that cellulose synthase activity influences microtubule cortical array organization. Plant Physiol 147: 1723–1734.
27. Hall DH, Gu G, Garcia-Anoveros J, Gong L, Chalfie M, et al. (1997) Neuropathology of degenerative cell death in Caenorhabditis elegans. J Neurosci 17: 1033–1045.
28. Ishigaki S, Liang Y, Yamamoto M, Niwa J, Ando Y, et al. (2002) X-Linked inhibitor of apoptosis protein is involved in mutant SOD1-mediated neuronal degeneration. J Neurochem 82: 576–584.
29. Katsuno M, Adachi H, Doyu M, Minamiyama M, Sang C, et al. (2003) Leuprorelin rescues polyglutamine-dependent phenotypes in a transgenic mouse model of spinal and bulbar muscular atrophy. Nat Med 9: 768–773.
30. Thomas JH (1990) Genetic analysis of defecation in Caenorhabditis elegans. Genetics 124: 855–872.
31. McIntire SL, Garriga G, White J, Jacobson D, Horvitz HR (1992) Genes necessary for directed axonal elongation or fasciculation in C. elegans. Neuron 8: 307–322.
32. Comley LH, Wishart TM, Baxter B, Murray LM, Nimmo A, et al. (2011) Induction of cell stress in neurons from transgenic mice expressing yellow fluorescent protein: implications for neurodegeneration research. PLoS One 6.
33. Sikorska B, Liberski PP, Giraud P, Kopp N, Brown P (2004) Autophagy is a part of ultrastructural synaptic pathology in Creutzfeldt-Jakob disease: a brain biopsy study. Int J Biochem Cell Biol 36: 2563–2573.
34. Nixon RA, Wegiel J, Kumar A, Yu WH, Peterhoff C, et al. (2005) Extensive involvement of autophagy in Alzheimer disease: an immuno-electron microscopy study. J Neuropathol Exp Neurol 64: 113–122.
35. Mizushima N, Yoshimori T, Levine B (2010) Methods in mammalian autophagy research. Cell 140: 313–326.
36. Melendez A, Levine B (2009) Autophagy in C. elegans. WormBook: 1–26.
37. Ohara S, Ukita Y, Ninomiya H, Ohno K (2004) Axonal dystrophy of dorsal root ganglion sensory neurons in a mouse model of Niemann-Pick disease type C. Exp Neurol 187: 289–298.
38. Noda T, Ohsumi Y (1998) Tor, a phosphatidylinositol kinase homologue, controls autophagy in yeast. J Biol Chem 273: 3963–3966.
39. You YJ, Kim J, Cobb M, Avery L (2006) Starvation activates MAP kinase through the muscarinic acetylcholine pathway in Caenorhabditis elegans pharynx. Cell Metab 3: 237–245.
40. Geeraert C, Ratier A, Pfisterer SG, Perdiz D, Cantaloube I, et al. (2010) Starvation-induced hyperacetylation of tubulin is required for the stimulation of autophagy by nutrient deprivation. J Biol Chem 285: 24184–24194.
41. Morselli E, Maiuri MC, Markaki M, Megalou E, Pasparaki A, et al. (2010) Caloric restriction and resveratrol promote longevity through the Sirtuin-1-dependent induction of autophagy. Cell Death Dis 1: e10.
42. Hansen M, Chandra A, Mitic LL, Onken B, Driscoll M, et al. (2008) A role for autophagy in the extension of lifespan by dietary restriction in C. elegans. PLoS Genet 4: e24.

43. Sarkar S, Krishna G, Imarisio S, Saiki S, O'Kane CJ, et al. (2008) A rational mechanism for combination treatment of Huntington's disease using lithium and rapamycin. Hum Mol Genet 17: 170–178.
44. Harrison DE, Strong R, Sharp ZD, Nelson JF, Astle CM, et al. (2009) Rapamycin fed late in life extends lifespan in genetically heterogeneous mice. Nature 460: 392–395.
45. Robida-Stubbs S, Glover-Cutter K, Lamming DW, Mizunuma M, Narasimhan SD, et al. (2012) TOR signaling and rapamycin influence longevity by regulating SKN-1/Nrf and DAF-16/FoxO. Cell Metab 15: 713–724.
46. Reed NA, Cai D, Blasius TL, Jih GT, Meyhofer E, et al. (2006) Microtubule acetylation promotes kinesin-1 binding and transport. Curr Biol 16: 2166–2172.
47. Dompierre JP, Godin JD, Charrin BC, Cordelieres FP, King SJ, et al. (2007) Histone deacetylase 6 inhibition compensates for the transport deficit in Huntington's disease by increasing tubulin acetylation. J Neurosci 27: 3571–3583.
48. Akella JS, Wloga D, Kim J, Starostina NG, Lyons-Abbott S, et al. (2010) MEC-17 is an alpha-tubulin acetyltransferase. Nature 467: 218-222.
49. Ori-McKenney KM, Xu J, Gross SP, Vallee RB (2010) A cytoplasmic dynein tail mutation impairs motor processivity. Nat Cell Biol 12: 1228–1234.
50. Ross JL, Wallace K, Shuman H, Goldman YE, Holzbaur EL (2006) Processive bidirectional motion of dynein-dynactin complexes in vitro. Nat Cell Biol 8: 562–570.
51. Haghnia M, Cavalli V, Shah SB, Schimmelpfeng K, Brusch R, et al. (2007) Dynactin is required for coordinated bidirectional motility, but not for dynein membrane attachment. Mol Biol Cell 18: 2081–2089.
52. Welte MA (2010) Bidirectional transport: matchmaking for motors. Curr Biol 20: R410–413.
53. Caccamo A, Majumder S, Deng JJ, Bai Y, Thornton FB, et al. (2009) Rapamycin rescues TDP-43 mislocalization and the associated low molecular mass neurofilament instability. J Biol Chem 284: 27416–27424.
54. Spilman P, Podlutskaya N, Hart MJ, Debnath J, Gorostiza O, et al. (2010) Inhibition of mTOR by rapamycin abolishes cognitive deficits and reduces amyloid-beta levels in a mouse model of Alzheimer's disease. PLoS One 5: e9979.
55. Zhang X, Li L, Chen S, Yang D, Wang Y, et al. (2011) Rapamycin treatment augments motor neuron degeneration in SOD1 (G93A) mouse model of amyotrophic lateral sclerosis. Autophagy 7.

nature COMMUNICATIONS

ARTICLE

Received 17 Sep 2012 | Accepted 20 Dec 2012 | Published 29 Jan 2013

DOI: 10.1038/ncomms2417

Heat shock factor-1 influences pathological lesion distribution of polyglutamine-induced neurodegeneration

Naohide Kondo[1], Masahisa Katsuno[1], Hiroaki Adachi[1], Makoto Minamiyama[1], Hideki Doi[1], Shinjiro Matsumoto[1], Yu Miyazaki[1], Madoka Iida[1], Genki Tohnai[1], Hideaki Nakatsuji[1], Shinsuke Ishigaki[1], Yusuke Fujioka[1], Hirohisa Watanabe[1], Fumiaki Tanaka[1], Akira Nakai[2] & Gen Sobue[1]

A crucial feature of adult-onset neurodegenerative diseases is accumulation of abnormal protein in specific brain regions, although the mechanism underlying this pathological selectivity remains unclear. Heat shock factor-1 is a transcriptional regulator of heat shock proteins, molecular chaperones that abrogate neurodegeneration by refolding and solubilizing pathogenic proteins. Here we show that heat shock factor-1 expression levels are associated with the accumulation of pathogenic androgen receptor in spinal and bulbar muscular atrophy, a polyglutamine-induced neurodegenerative disease. In heterozygous *heat shock factor-1*-knockout spinal and bulbar muscular atrophy mice, abnormal androgen receptor accumulates in the cerebral visual cortex, liver and pituitary, which are not affected in their genetically unmodified counterparts. The depletion of *heat shock factor-1* also expands the distribution of pathogenic androgen receptor accumulation in other neuronal regions. Furthermore, lentiviral-mediated delivery of heat shock factor-1 into the brain of spinal and bulbar muscular atrophy mice topically suppresses the pathogenic androgen receptor accumulation and neuronal atrophy. These results suggest that heat shock factor-1 influences the pathological lesion selectivity in spinal and bulbar muscular atrophy.

[1] Department of Neurology, Nagoya University Graduate School of Medicine, Nagoya 466-8550, Japan. [2] Department of Biochemistry and Molecular Biology, Yamaguchi University School of Medicine, Ube 755-8505, Japan. Correspondence and requests for materials should be addressed to M.K. (email: ka2no@med.nagoya-u.ac.jp).

Heat shock proteins (Hsps), including Hsp70 and Hsp40, are stress-induced molecular chaperones that have important roles in maintaining correct folding, the assembly of newly synthesized proteins and the intracellular transport of proteins[1,2]. There are various lines of evidence indicating that Hsps abrogate neurodegeneration by refolding and solubilizing pathogenic proteins[3,4]. Particularly, Hsp70 facilitates the proteasomal degradation of abnormal proteins and thereby ameliorates neuronal damage in cellular and animal models of adult-onset neurodegenerative disorders, including Alzheimer's disease, amyotrophic lateral sclerosis and Huntington' disease (HD)[5–7] and other polyglutamine diseases caused by the expansion of a genomic CAG repeat[8–10]. Among several molecules that control the expression of Hsps, heat shock factor-1 (Hsf-1) is shown to strongly regulate the expression of Hsp70 by activating its promoter[11,12].

To develop effective treatments for neurodegenerative disorders, it is important to elucidate the molecular mechanism by which only specific cells are affected, despite the broad expression of the disease-causing mutant genes. The selectivity of the pathogenic lesions in neurodegenerative diseases may be influenced by several factors. For example, the length of the CAG triplet repeat in the causative gene influences the distribution of pathological lesions of spinocerebellar ataxia type 7 and dentatorubral pallidoluysian atrophy[13,14]. Given that the length of the polyglutamine tract increases the propensity of the protein to aggregate, the pathological lesion selectivity of spinocerebellar ataxia type 7 appears to be influenced by the biological properties of the causative protein[15]. Alternatively, the expression of molecules that interact with the disease-causing proteins, such as PQBP-1 and Rhes, is also associated with the distribution of selective neuronal cell loss in polyglutamine diseases[16,17]. Furthermore, transcriptional factors such as nuclear transcription factor Y subunit alpha (NF-YA) and p53 were shown to, at least partially, determine the vulnerability of cells to polyglutamine-expanded proteins by regulating the expression of Hsps in cellular models of HD[18,19].

The accumulation of polyglutamine-expanded proteins is detected histopathologically as diffuse nuclear staining or as intraneuronal inclusion bodies, the distribution of which corresponds to that of pathological involvement and symptomatic phenotypes[20,21]. The intranuclear accumulation of disease-causing misfolded proteins is thought to trigger neurodegeneration by various mechanisms such as transcriptional dysregulation, impairment of axonal transport and mitochondrial dysfunction[22–24]. This view is supported by animal studies showing that the prevention of pathogenic protein accumulation successfully rescues the phenotype in model mice of polyglutamine diseases[25–28].

Here, we investigated the role of Hsf-1 in pathogenic lesion selectivity in spinal and bulbar muscular atrophy (SBMA), an adult-onset motor neuron disease caused by the expansion of a CAG repeat in the gene coding androgen receptor (AR)[29–31]. This disease affects susceptible regions, such as spinal anterior horn, brainstem and pancreas, despite the ubiquitous expression of the causative protein[32]. In the present study, we found that the heterozygous knockout of *Hsf-1* in SBMA model mice led to the extended distribution of pathogenic AR accumulation in neuronal and non-neuronal tissues as well as exacerbated neuromuscular phenotype, whereas the lentiviral overexpression of HSF-1 locally precludes pathogenic AR accumulation and neuronal atrophy in the brain of the SBMA mice.

Results

Hsf-1 levels are associated with pathogenic AR accumulation. To examine whether the expression levels of Hsf-1 are associated with the distribution of pathogenic AR accumulation in SBMA, we performed immunohistochemistry on the central nervous system (CNS) of a transgenic SBMA mouse model carrying human AR with 97 CAGs (AR-97Q). In this model animal, the full-length human AR was expressed ubiquitously (Supplementary Fig. S1a). The results showed that low expression levels of Hsf-1 were associated with a high frequency of pathogenic AR accumulation (Fig. 1a,b). For example, the accumulation of pathogenic AR is frequently observed in spinal motor neurons that show weak immunoreactivity for Hsf-1. In contrast, neurons in the cerebral cortex and striatum, most of which are Hsf-1-positive, were rarely stained with 1C2, a specific antibody against the expanded polyglutamine tract. In the cerebellum of AR-97Q mice, there was a scarce accumulation of pathogenic AR in Purkinje cells, where Hsf-1 was expressed at a high level. Conversely, there were abundant 1C2-positive cells in the cerebellar granular cell layer, which showed scarce immunoreactivity for Hsf-1 (Fig. 1a). There was little difference in the expression pattern of Hsf-1 between AR-97Q and wild-type mice, except for the spinal anterior horn, where the nuclear expression of Hsf-1 was decreased in AR-97Q mice compared with wild-type mice (Fig. 1a). Quantitative analysis of the relationship between the expression levels of Hsf-1 and the frequency of 1C2-positive cells in various parts of the CNS confirmed that higher expression levels of Hsf-1 are associated with the reduced accumulation of pathogenic AR (Fig. 1b). This relationship, however, was not clearly observed for Nfya, p53, TATA box-binding protein (Tbp) or Sp1, which are other potential inducers of Hsp70 (Supplementary Fig. S1b,c). These findings led us to focus on Hsf-1 as a possible regulator of the pathogenic lesion selectivity, especially in the CNS, of the SBMA model mouse.

Previous studies showed that AR-97Q mice show pathogenic AR aggregation in non-neuronal tissues, such as the heart, lung, pancreas and skeletal muscle, in addition to the CNS[25]. To examine whether the expression levels of Hsf-1 are also associated with pathogenic AR accumulation outside the CNS, we performed immunohistochemistry using anti-Hsf-1 and 1C2 antibodies on non-neuronal tissues of the AR-97Q mice. The results demonstrated that a similar relationship as seen in CNS was observed in the pancreas, liver and testis. There was unequivocal pathogenic AR accumulation in the pancreas, where Hsf-1 is expressed at a low level (Supplementary Fig. S1d). In contrast, no visible pathogenic AR accumulation was observed in the liver or testis, where Hsf-1 is expressed at a relatively high level (Supplementary Fig. S1d).

We further verified this relationship in autopsied specimens from SBMA patients. 1C2-positive cells were frequently detected in spinal motor neurons and pancreatic islet cells, where HSF-1 is expressed at a low level, compared with control subjects. In contrast, there were no 1C2-stained cells in the neuronal and non-neuronal tissues in which HSF-1 was expressed at a high level (Supplementary Fig. S2a,b).

Taken together, these results indicate that high expression levels of Hsf-1 are associated with reduced pathogenic AR accumulation in neuronal and non-neuronal tissues of the SBMA mouse model and SBMA patients.

***Hsf-1* depletion expands distribution of AR accumulation.** To clarify whether low expression levels of Hsf-1 have a causative role in the accumulation of pathogenic AR *in vivo*, we depleted *Hsf-1* in AR-97Q mice by crossing them with heterozygous *Hsf-1*-knockout mice[33]. As *Hsf-1*-null AR-97Q (AR-97Q Tg/−, *Hsf-1* −/−) mice were not obtained, presumably owing to their early death during embryonic development, we performed immunohistochemistry on various tissues from wild-type

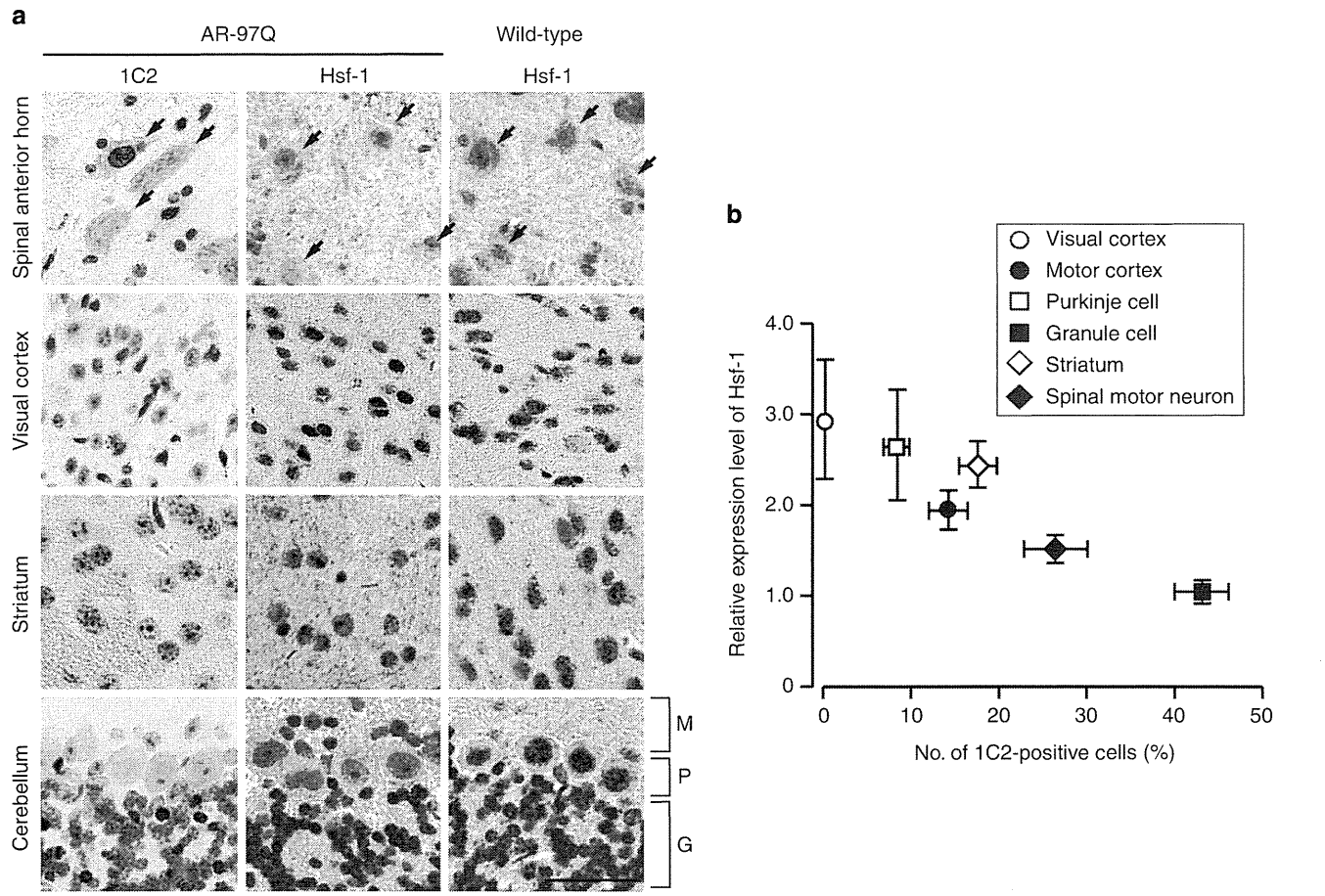

Figure 1 | Hsf-1 expression is associated with pathogenic AR accumulation. (**a**) Immunohistochemistry for Hsf-1 and expanded polyglutamine (1C2) in the spinal anterior horn, visual cortex, striatum and cerebellum from wild-type and AR-97Q mice (13 weeks old). Arrows indicate motor neurons within the spinal anterior horn. M, molecular layer; P, Purkinje cell layer; G, granular layer. (**b**) Quantification of the relationship between the nuclear immunoreactivity of Hsf-1 and the frequency of 1C2-positive cells in different parts of the CNS. More than 500 neurons in each part from three brains were analysed (**b**). Error bars indicate s.e.m. (**b**). Scale bars, 50 μm (**a**).

(AR-97Q −/−, *Hsf-1* +/+), AR-97Q (AR-97Q Tg/−, *Hsf-1* +/+) and heterozygous *Hsf-1*-knockout AR-97Q (AR-97Q Tg/−, *Hsf-1* +/−) mice, to examine whether Hsf-1 inactivation expands the distribution of pathogenic AR accumulation. The nuclear accumulation of pathogenic AR is not detected in the liver and pituitary gland of AR-97Q mice, even at an advanced stage (Supplementary Fig. S3). Surprisingly, we observed the nuclear accumulation of pathogenic AR in the liver of the heterozygous *Hsf-1*-knockout SBMA mice (Fig. 2a). Quantitative analysis showed that 1.40 ± 0.35% (1.0–2.1) of hepatocytes were positive for 1C2 in the *Hsf-1*-depleted AR-97Q mice, while no positive cells were observed in the AR-97Q mice ($n = 3$ per group). To confirm the effects of *Hsf-1* depletion on the metabolism of pathogenic AR, we performed immunoblotting of the liver samples using an anti-AR antibody. The results revealed that the expression level of AR monomer, which appears to be one of the toxic species of polyglutamine protein[34], was increased by the heterozygous knockout of *Hsf-1* in the liver of AR-97Q mice (Fig. 2b,c). Insoluble high-molecular-weight AR complexes, which may have a protective property, were not detected in the liver of either type of mice, presumably because of the relatively low expression levels of AR in this tissue.

To assess whether the accumulation of pathogenic AR due to *Hsf-1* depletion impairs liver function, we performed histology and blood tests on each mouse group. The serum levels of liver enzymes, such as aspartate aminotransferase and alanine aminotransferase, which are indicative of liver dysfunction, were significantly elevated in heterozygous *Hsf-1*-knockout AR-97Q mice compared with the genetically unmodified AR-97Q mice (Fig. 2d,e), while this was not the case for wild-type mice (Fig. 2f,g). Furthermore, immunohistochemistry demonstrated that the liver became atrophied in the heterozygous *Hsf-1*-knockout AR-97Q mice, but not in their wild-type counterparts (Fig. 2h–j). Similarly, pathogenic AR accumulation was also detected in the pituitary gland of the heterozygous *Hsf-1*-knockout SBMA mice (Fig. 2a). A total of 0.67 ± 0.17% (0.5–1.0) of the cells in the pituitary gland of the heterozygous *Hsf-1*-knockout AR-97Q mice exhibited the nuclear accumulation of pathogenic AR, although there were no 1C2-positive cells in the pituitary gland of genetically unmodified AR-97Q mice ($n = 3$ per group). These findings indicate that Hsf-1 prevents the accumulation of pathogenic AR in the liver and pituitary gland of AR-97Q mice.

A similar phenomenon was observed in certain parts of the CNS in AR-97Q mice. Interestingly, the accumulation of pathogenic AR was detected in the cerebral visual cortex of heterozygous *Hsf-1*-knockout SBMA mice (Fig. 3a), where the accumulation of pathogenic AR was not observed in the AR-97Q mice, even at an advanced stage (Supplementary Fig. S3). Furthermore, the heterozygous knockout of *Hsf-1* also augmented the accumulation of pathogenic AR in spinal motor neurons and Purkinje cells as well as the neurons of the striatum

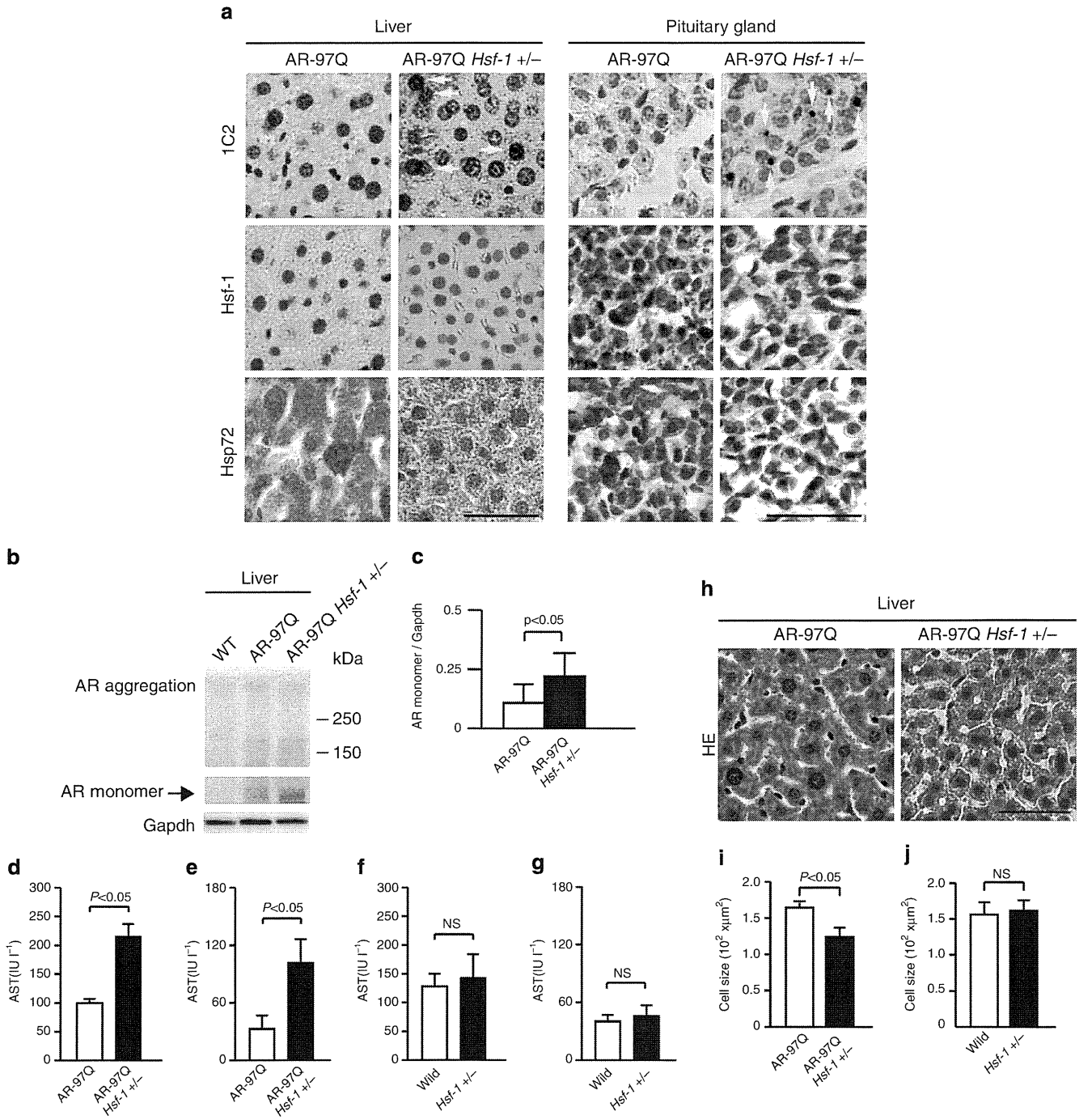

Figure 2 | Pathogenic AR accumulates in the liver and pituitary gland of heterozygous *Hsf-1*-knockout AR-97Q mice. (**a**) Immunohistochemistry of AR-97Q and *Hsf-1*-knockout AR-97Q mice using anti-Hsf-1, anti-Hsp72 and anti-polyglutamine (1C2) antibodies (13 weeks old). The *Hsf-1*-knockout AR-97Q mice showed the nuclear accumulation of pathogenic AR (yellow arrows) and decreased levels of Hsf-1 and Hsp72, an inducible form of Hsp70, in the liver and pituitary gland. (**b**) Immunoblotting for AR in wild-type, AR-97Q and *Hsf-1*-knockout AR-97Q mice (13 weeks old). (**c**) Quantification of immunoblotting revealed that the expression levels of AR monomer were upregulated in the liver of heterozygous *Hsf-1*-knockout AR-97Q mice. Unpaired *t*-test, $n = 3$. (**d**–**g**) Blood tests revealed that the liver enzyme levels, including aspartate aminotransferase (AST) (**d**) and alanine aminotransferase (ALT) (**e**), were elevated in heterozygous *Hsf-1*-knockout AR-97Q mice compared with AR-97Q mice (13 weeks old). There were no significant differences in the levels of AST (**f**) and ALT (**g**) between wild-type and heterozygous *Hsf-1*-knockout mice (13 weeks old). (**h**) Haematoxylin-eosin staining of the liver of heterozygous *Hsf-1*-knockout and genetically unmodified AR-97Q mice (13 weeks old). (**i**) Quantitative analysis showed that the size of hepatocytes was reduced in heterozygous *Hsf-1*-knockout AR-97Q mice compared with AR-97Q mice. (**j**) Depletion of *Hsf-1* did not alter the size of hepatocytes in wild-type mice. Unpaired *t*-test ($n = 4$) (**d**–**g**). More than 1,000 cells from three livers were analysed in each group, unpaired *t*-test. (**i**,**j**). Error bars indicate s.e.m. (**c**–**g**,**i**,**j**). Scale bars, 50 μm (**a**,**h**). NS, not significant.

through Hsp70 downregulation (Fig. 3a and Supplementary Fig. S4a). Quantitative analysis of the change in the relationship between the Hsf-1 expression levels and the frequency of 1C2-positive cells confirmed that the accumulation of pathogenic AR was significantly increased by the heterozygous depletion of Hsf-1 (Fig. 3b–e). Although pathogenic AR mainly

accumulated in the fifth and sixth layers of the cerebral motor cortex in the AR-97Q mice, where the expression levels of Hsf-1 are relatively lower than in the other layers, the distribution of pathogenic AR accumulation was expanded to the second and third layers in the heterozygous *Hsf-1*-knockout AR-97Q mice (Fig. 3f). The heterozygous knockout of *Hsf-1* also altered the distribution and frequency of pathogenic AR accumulation in neuronal and non-neuronal tissues in the AR-97Q mice (Supplementary Fig. S4b and Supplementary Table S1). To verify the impact of *Hsf-1* depletion upon the pathogenic AR aggregations, we next analysed immunoblots of the spinal cord, cerebral cortex, striatum and cerebellum using an anti-AR antibody. The findings showed that the amount of smearing AR protein, which corresponds to the toxic oligomers, was increased by the heterozygous depletion of *Hsf-1* in each part of the CNS of the AR-97Q mice (Fig. 3g–i). These findings suggest that Hsf-1 expression levels influence the degree of pathogenic AR accumulation in the SBMA mouse model.

***Hsf-1* depletion aggravates neurodegeneration in SBMA mice.** To examine whether the decreased expression levels of Hsf-1 leads to increased motor neuronal damage in the SBMA mouse model, we analysed the effects of *Hsf-1* depletion on the neurological and histopathological phenotypes of AR-97Q mice. The results demonstrated that muscle atrophy was enhanced in the *Hsf-1*-knockout AR-97Q mice compared with the genetically unmodified AR-97Q mice (Fig. 4a and Supplementary Movie 1). Footprint analysis showed that the stride length was shortened and the paws were dragged in the heterozygous *Hsf-1*-knockout AR-97Q mice (Fig. 4b,c). The heterozygous knockout of *Hsf-1* in AR-97Q mice also shortened their lifespan and decreased their body weight, and also exacerbated muscle weakness, as measured using grip power and the rotarod task (Fig. 4d–g). To exclude nonspecific effects of *Hsf-1* depletion on the motor phenotypes of wild-type mice, we investigated the lifespan and motor function of heterozygous *Hsf-1*-knockout wild-type mice (Supplementary Fig. S5a–d). The results showed that the heterozygous knockout of *Hsf-1* had no influence on the lifespan, body weight or motor function of wild-type mice, suggesting that the deleterious effects of *Hsf-1* depletion are disease-specific phenomena.

To investigate the neuropathological changes underlying the phenotypic aggravation and the increase of pathogenic 1C2-positive neuronal cells, we performed immunohistochemistry on the spinal anterior horn, cerebral cortex, striatum and cerebellum of heterozygous *Hsf-1*-knockout and genetically unmodified AR-97Q mice using antibodies against choline acetyl transferase (ChAT), NeuN and calbindin. The results showed that neurons in each part of the CNS were atrophied in the *Hsf-1*-knockout AR-97Q mice (Fig. 5a–h). Western blot analysis confirmed the decreased levels of ChAT, a functional marker of spinal motor neurons, in the heterozygous *Hsf-1*-knockout AR-97Q mice (Fig. 5i,j).

To analyse the effects of *Hsf-1* depletion on the denervation at neuromuscular junctions (NMJs) of AR-97Q mice, we performed immunofluorescent staining of NMJs using α-bungarotoxin together with antibodies against synaptophysin and phospho neurofilament (Fig. 5k). Quantitative analysis showed that the frequency of denervation at NMJ is increased in the heterozygous *Hsf-1*-knockout SBMA mice compared with the AR-97Q mice (Fig. 5l). In addition, immunohistochemistry and immunoblot analysis using an antibody against glial fibrillary acid protein (GFAP) showed increased immunoreactivity in the anterior horn of the spinal cord of the heterozygous *Hsf-1*-knockout SBMA mice compared with AR-97Q mice, indicating that motor neuron degeneration was enhanced by the partial depletion of *Hsf-1* (Fig. 5m–p). Furthermore, haematoxylin and eosin staining demonstrated that skeletal muscle fibres were atrophied in the heterozygous *Hsf-1*-knockout AR-97Q mice compared with the genetically unmodified AR-97Q mice, suggesting the aggravation of neurogenic amyotrophy (Supplementary Fig. S6a,b).

Tissue-specific regulation of Hsps in SBMA mice. To confirm that the heterozygous knockout of *Hsf-1* leads to the downregulation of Hsps, we performed immunoblotting on several tissues from each mouse group. We found that the degree of Hsf-1 downregulation differed in a tissue-specific manner in the heterozygous *Hsf-1*-knockout SBMA mice. For example, the protein levels of Hsf-1 were significantly decreased by the heterozygous knockout of *Hsf-1* in the spinal cord, liver and skeletal muscle (Fig. 6a–d). Conversely, the expression levels of Hsf-1 were not changed in the testis of the heterozygous *Hsf-1*-knockout AR-97Q mice compared with the AR-97Q mice (Fig. 6a,e). In accordance with these findings, Hsp72, the inducible form of Hsp70, was downregulated in the spinal cord and liver, but not in the testis, of the heterozygous *Hsf-1*-knockout AR-97Q mice (Fig. 6a–c,e). Moreover, Hsp105 was also significantly downregulated in the spinal cord and liver of the heterozygous *Hsf-1*-knockout mice (Fig. 6a–c). However, the expression levels of Hsps within skeletal muscle were not changed by *Hsf-1* depletion (Fig. 6a,d). Similar findings were observed in the heterozygous *Hsf-1*-knockout wild-type mice compared with wild-type mice (Supplementary Fig. S7a–d). To confirm that the downregulation of Hsp72 following *Hsf-1* depletion was via the decrease of messenger RNA levels, we analysed the mRNA expression levels of *Hsp70A1*, the gene encoding Hsp72, in the spinal cord, liver and skeletal muscle. The results showed that the mRNA levels of *Hsp70A1* were decreased in the spinal cord and liver of the heterozygous *Hsf-1*-knockout AR-97Q mice, in agreement with the immunoblotting findings (Fig. 6f,g). In contrast, the heterozygous knockout of *Hsf-1* did not alter the mRNA levels of *Hsp70A1* in skeletal muscle (Fig. 6h). There were no detectable changes in the expression levels of Hsp40 and Hsp90 in all the tissues examined from heterozygous Hsf-1-knockout AR-97Q mice (Fig. 6a–e). These findings are compatible with the change in the distribution of pathogenic AR accumulation, and indicate that the induction of Hsp70 is dependent on the expression levels of Hsf-1 in the spinal cord and liver, but not in the skeletal muscle, of the SBMA model mice.

To elucidate the molecular machinery underlying the Hsf-1-independent regulation of Hsp70 expression in the skeletal muscle of AR-97Q mice, we investigated the expression levels of several major transcription factors, such as Nfya, Tbp, p53 and Sp1, which also regulate the expression of Hsp70 (refs 18,19, 35–37). The results showed that Nfya and Sp1, but not Tbp nor p53, were upregulated in the skeletal muscle of AR-97Q mice compared with wild-type mice (Fig. 7a). This upregulation was further enhanced by the partial depletion of *Hsf-1* (Fig.7a–c). In contrast to the skeletal muscle, neither Nfya nor Sp1 were upregulated by *Hsf-1* depletion in the spinal cord or liver of AR-97Q mice (Fig. 7d,e). Immunohistochemical analysis showed an increase in the levels of nuclear Nfya and Sp1 in the skeletal muscle of AR-97Q mice, which was further intensified by the heterozygous knockout of *Hsf-1* (Fig. 7f–h). These findings suggest that proteins such as Nfya and Sp1 appear to regulate the expression of Hsp70 and this probably underlies the observation that pathogenic AR accumulation was not increased in the skeletal muscle of the *Hsf-1*-depleted AR-97Q mice.

To investigate the effects of Hsf-1 on the pathogenic AR aggregations in the skeletal muscle, we analysed immunoblots of

the tissue using an anti-AR antibody. The results showed that the amount of oligomers or monomer of pathogenic AR was not increased by the heterozygous depletion of *Hsf-1* in the skeletal muscle of AR-97Q mice (Fig. 7i,j). In agreement with these immunoblot analyses, immunohistochemistry demonstrated no significant difference in the number of 1C2-positive cells

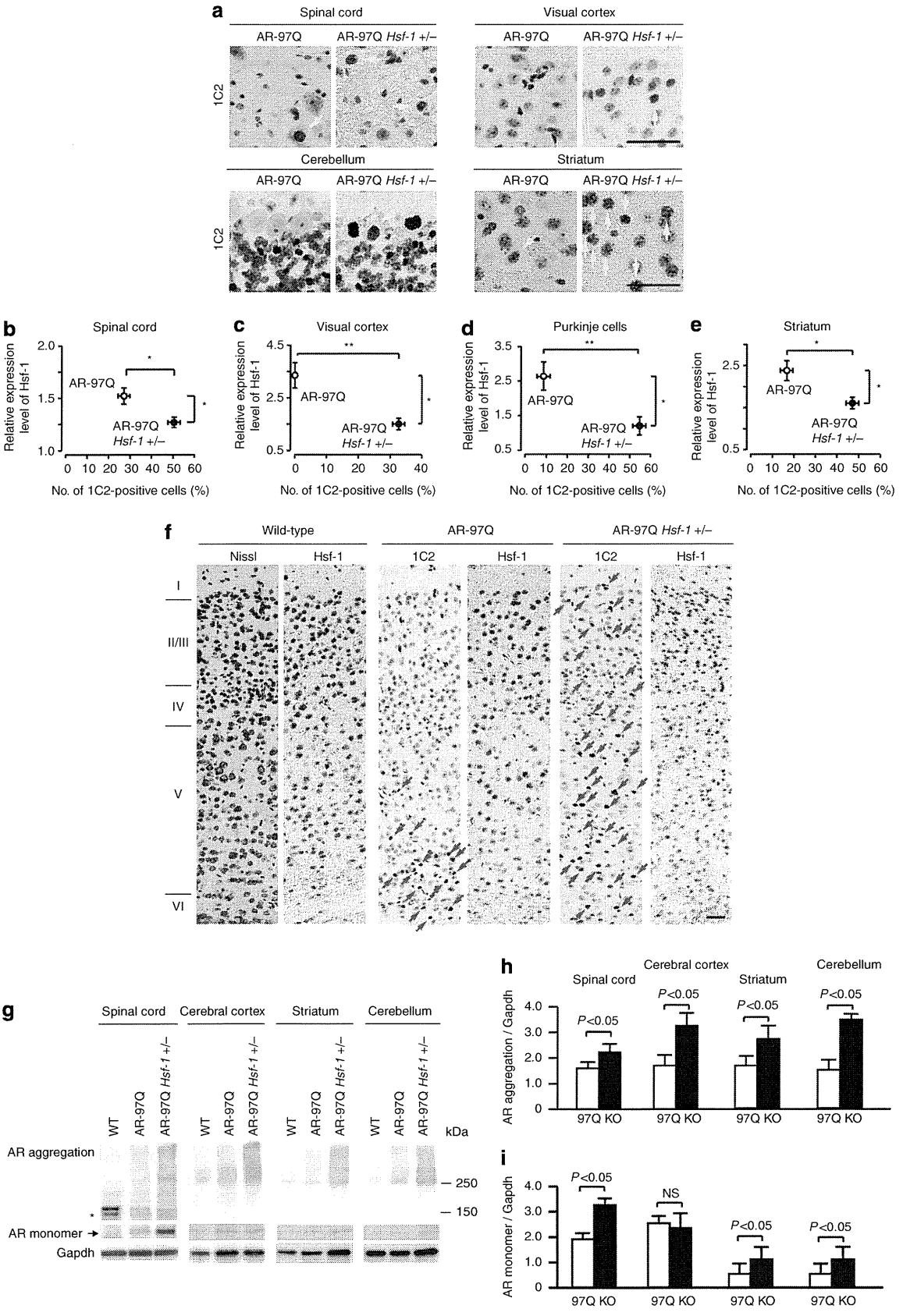

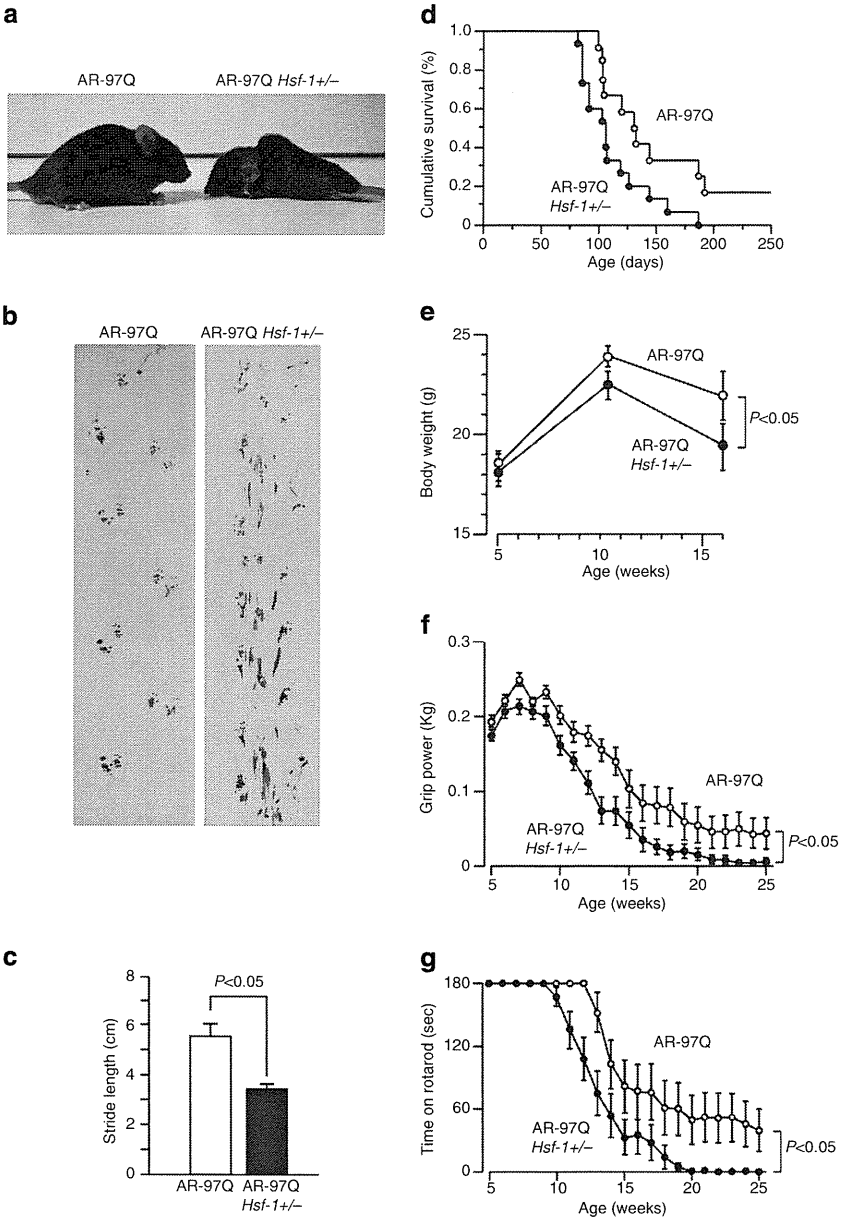

Figure 4 | Heterozygous *Hsf-1*-knockout AR-97Q mice have more severe muscle atrophy than AR-97Q mice. (**a**) Muscle atrophy is enhanced in the *Hsf-1*-knockout AR-97Q mice compared with the AR-97Q mice (10 weeks old). (**b**) Footprints of 13-week-old AR-97Q and *Hsf-1*-knockout AR-97Q mice. The front paws are shown in red, while the hind paws are shown in blue. (**c**) Quantification of the footprints revealed that the stride length was significantly shortened in the heterozygous *Hsf-1*-knockout AR-97Q mouse (13 weeks old). Unpaired *t*-test ($n=3$). Cumulative survival (**d**), body weight (**e**), grip power (**f**) and Rotarod task (**g**) of AR-97Q and *Hsf-1*-knockout AR-97Q mice. There were significant differences in all parameters between the AR-97Q ($n=12$) and heterozygous *Hsf-1*-knockout AR-97Q ($n=15$) mice by unpaired *t*-test: $P<0.05$ (**d**); $P<0.05$ at 16 weeks (**e**); $P<0.05$ at 25 weeks (**f**); and $P<0.05$ at 25 weeks (**g**). Error bars indicate s.e.m. (**c**–**g**).

Figure 3 | Augmentation of pathogenic AR accumulation in the CNS of *Hsf-1*-knockout AR-97Q mice. (**a**) Immunohistochemistry for 1C2, Hsf-1 and Hsp72 in AR-97Q and *Hsf-1*-knockout AR-97Q mice (13 weeks old). Pathogenic AR (yellow arrows) accumulated in the cerebral visual cortex of heterozygous *Hsf-1*-knockout SBMA mice where the accumulation of pathogenic AR was not observed in the AR-97Q mice. (**b**–**e**) The change in the relationship between the expression levels of Hsf-1 and the frequency of 1C2-positive neurons in the spinal anterior horn (**b**), cerebral visual cortex (**c**), Purkinje cells of the cerebellum (**d**) and striatum (**e**). (**f**) Immunohistochemistry for Hsf-1 and 1C2 in the cerebral motor cortex of AR-97Q and *Hsf-1*-knockout AR-97Q mice (13 weeks old). In AR-97Q mice, 1C2-positive cells were observed in the fifth layer of the cerebral motor cortex, where the expression levels of Hsf-1 were relatively lower than in the other layers. The distribution of pathogenic AR accumulation (red arrows) was expanded to the second and third layers of the cerebral motor cortex in heterozygous *Hsf-1*-knockout AR-97Q mice. (**g**) Immunoblotting for AR in wild-type, AR-97Q and *Hsf-1*-knockout AR-97Q mice (13 weeks old). Pathogenic AR oligomers are indicated by a smear from the top of the gel. *Nonspecific bands. (**h**) Quantitative analysis of immunoblots using densitometry indicated that the expression levels of abnormal AR protein complexes in the spinal cord, cerebral cortex, striatum and cerebellum were upregulated in heterozygous *Hsf-1*-knockout AR-97Q mice compared with AR-97Q mice. (**i**) Quantification of immunoblotting revealed that the expression levels of AR monomer were upregulated in the spinal cord, striatum and cerebellum of heterozygous *Hsf-1*-knockout AR-97Q mice. $^*P<0.05$, $^{**}P<0.01$ by unpaired *t*-test. More than 500 neurons from three brains were analysed in each group (**b**–**e**). Unpaired *t*-test ($n=3$) (**h**,**i**). Error bars indicate s.e.m. (**b**–**e**,**h**,**i**). Scale bars, 50 μm (**a**). NS, not significant.

in the skeletal muscle between the heterozygous *Hsf-1*-knockout and genetically unmodified AR-97Q mice (Supplementary Fig. S8a,b).

Overexpression of Hsf-1 suppresses AR accumulation. To investigate whether Hsf-1 exerts neuroprotection in the mouse model of SBMA, we administered a lentiviral vector expressing

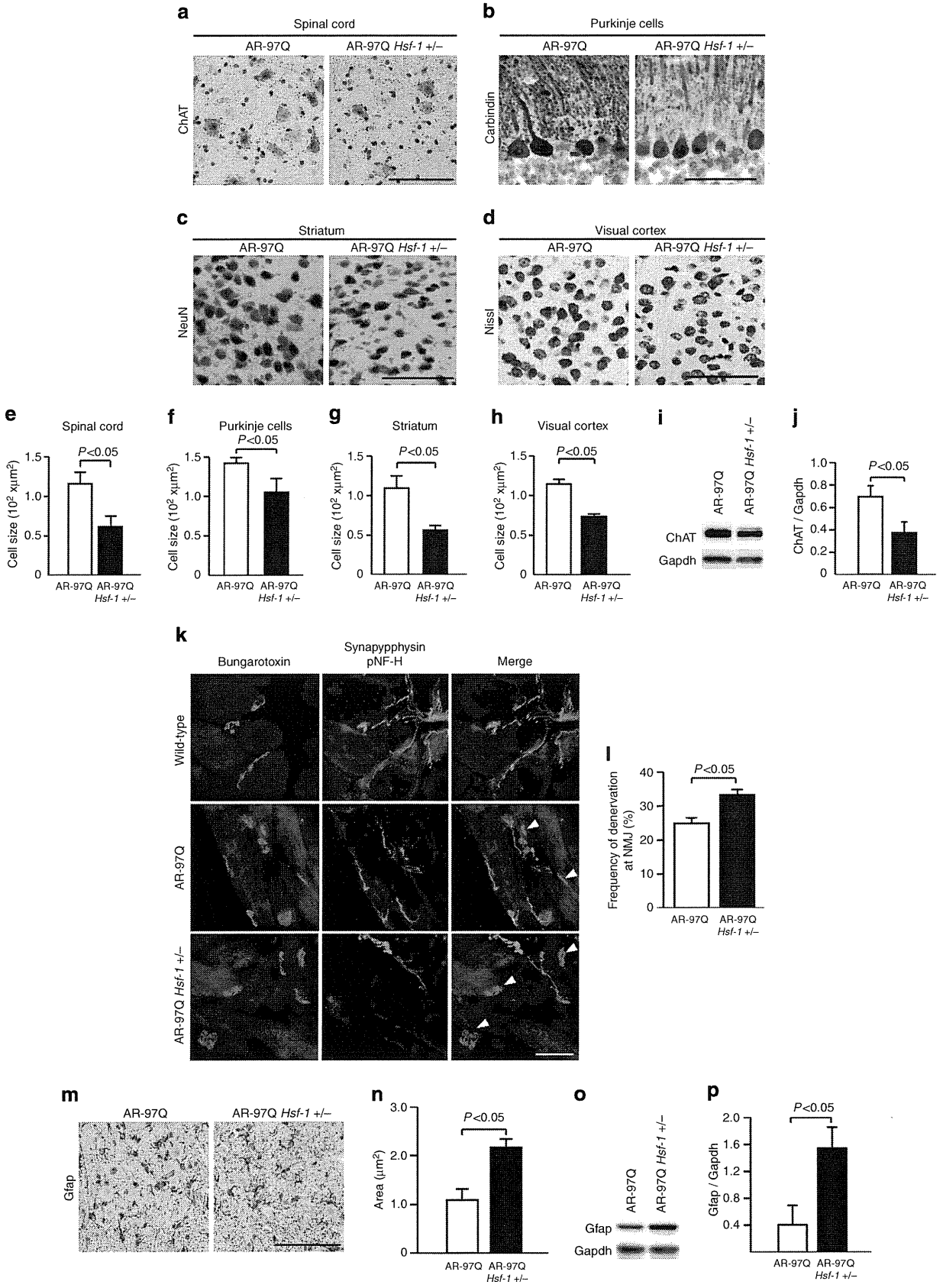

green fluorescent protein (GFP) with or without human HSF-1 into the motor cortex and striatum of the AR-97Q mice (Fig. 8a,f), as previous reports showed that no line of transgenic mice of HSF-1 demonstrates an increased expression level of this protein in the brain[38]. We performed stereotaxic injection of the lentiviral vector into the motor cortex or striatum of 8-week-old SBMA mice. Three weeks after the surgery, neuronal size and frequency of abnormal AR accumulation were examined. In both the motor cortex and striatum, the frequency of pathogenic AR accumulation around the lentiviral vector-injected area where HSF-1 was highly expressed was decreased in comparison with that in the contralateral side without treatment (Fig. 8b,g). In addition, the neuron sizes of the motor cortex and striatum were significantly increased by the *HSF-1* injecteion (Fig. 8b,g). Quantitative analyses confirmed these findings, whereas the lentiviral delivery of GFP without HSF-1 failed to show any neuroprotective effects (Fig. 8c–e,h–j and Supplementary Fig. S9a–j). These results indicated that HSF-1 overexpression attenuated the accumulation of pathogenic AR and eventual neurodegeneration in the brain of the SBMA mice.

In summary, we showed that the expression level of Hsf-1 influences the nuclear accumulation of pathogenic AR, and that the depletion of this transcription factor leads to the expanded distribution of pathological lesions and phenotypic exacerbation in the SBMA mouse model. However, these phenomena were not observed in skeletal muscle, where alternative regulators of Hsps, such as Nfya and Sp1, were upregulated. In addition, exogenous overexpression of HSF-1 using a lentivirus vector protected the neurons within the susceptible lesions of SBMA mice. Our results suggest that Hsf-1 contributes to the pathological lesion selectivity in SBMA, and that the tissue-specific regulation of Hsps should be taken into account for the development of therapies that induce the expression of molecular chaperones.

Discussion

In the present study, the heterozygous knockout of *Hsf-1* substantially augmented the nuclear accumulation of pathogenic AR in the CNS, suppressed the intraneuronal expression of Hsp70, diminished the size of affected neurons and exacerbated the neurological symptoms in a mouse model of SBMA. By contrast, the lentiviral delivery of HSF-1 attenuated pathogenic AR accumulation and neuronal atrophy in the brain of the SBMA mice. Hsps, particularly Hsp70, have a protective role in neurodegeneration by preventing the accumulation of abnormal proteins[4,39–43]. However, the role of Hsf-1 in the induction of Hsps is controversial in experiments using cellular models of polyglutamine diseases[18,19,38,44]. The results of the present study demonstrate that the expression of Hsp70, but not Hsp40, is regulated by Hsf-1 in various neurons including spinal motor neurons in the SBMA mouse model. As for the neuroprotective properties of Hsf-1 against cellular stresses, several studies showed that the overexpression of Hsf-1 suppresses the toxicity of polyglutamine-expanded proteins in cultured cells and rodents[38,44]. The present study also demonstrated the neuroprotective effects of the exogenous HSF-1 in the CNS of SBMA model mice. By contrast, the depletion of *Hsf-1* shortens the lifespan of a mouse model of HD, although the associated histopathological and biochemical alterations were not thoroughly examined[33]. Taken together, our findings indicate that the Hsf-1–Hsp70 pathway exerts neuroprotective effects via the suppression of pathogenic protein accumulation in the pathogenesis of polyglutamine-induced neurodegeneration.

The most intriguing finding of the present study is that the heterozygous depletion of *Hsf-1* altered the histopathological distribution of pathogenic AR accumulation in the AR-97Q mice, indicating a role for Hsf-1 in the selectivity of the pathogenic lesions in SBMA. The selective damage of specific subgroups of neuronal and non-neuronal cells, despite the ubiquitous expression of the causative protein, is a characteristic of neurodegenerative diseases, although the molecular mechanisms underlying this phenomenon remain unclear[23]. In patients with SBMA, the accumulation of pathogenic AR in each tissue corresponds to their clinical symptoms and findings, for example, lower motor neurons for muscle weakness and atrophy, and the pancreas for diabetes. Nevertheless, the distribution of pathogenic AR accumulation is not equivalent to the expression pattern of normal AR[20,32]. Furthermore, the accumulation of pathogenic AR is observed in specific tissues of the AR-97Q mice, although the expression of the transgene, which was regulated by a potent chicken-β-actin promoter, was also detected in tissues that showed no histopathological abnormalities[25,45]. These findings suggest that factors other than the transcription of mutant *AR* may contribute to the tissue-specific accumulation of the causative protein. In the present study, the heterozygous knockout of *Hsf-1* induced pathogenic AR accumulation in the cerebral visual cortex, liver and pituitary gland, which were not affected in genetically unmodified AR-97Q mice. In addition, the reduction of Hsf-1 expression in hepatocytes resulted in the exacerbation of liver dysfunction and cellular atrophy in the SBMA mouse model. Given that the defect of protein turnover leads to cellular atrophy[46], the impairment of protein quality control due to pathological AR accumulation induced by *Hsf-1* depletion may underlie the hepatocyte atrophy[47]. These findings indicate that endogenous Hsf-1 can clear certain lesions, such as in the cerebral visual cortex, liver and pituitary gland, of pathogenic AR accumulation and that the expression levels of Hsf-1 in each tissue, at least partially, influence the pathogenic lesion selectivity of SBMA.

Figure 5 | Histopathological change in the CNS of *Hsf-1*-knockout AR-97Q mice. (**a**–**d**) Histopathological analyses of AR-97Q and *Hsf-1*-knockout AR-97Q mice (13 weeks old). Immunohistochemistry for ChAT in the anterior horn of the spinal cord (**a**). Immunohistochemistry for calbindin in Purkinje cells (**b**). Immunohistochemistry for NeuN in the striatum (**c**). Nissl staining of the cerebral cortex (**d**). (**e**–**h**) Quantitative analysis of the size of neurons revealed that the neurons in each part of the CNS became atrophied in the *Hsf-1*-knockout AR-97Q mice compared with the AR-97Q mice. (**i**) Immunoblotting for ChAT in the spinal cord of AR-97Q and *Hsf-1*-knockout AR-97Q mice (13 weeks old). (**j**) Quantitative analysis of the signal intensity of the ChAT-immunoreactive bands. (**k**) Immunofluorescent staining of NMJs in 13-week-old AR-97Q and heterozygous *Hsf-1*-knockout AR-97Q mice (red, bungarotoxin; green, synaptophysin and phopsho-neurofilament H).The terminal of motor axons (green) are merged with virtually all the acetylcholine receptors labelled by bungarotoxin (red) in wild-type mice, indicating that NMJs are fully innervated. By contrast, some NMJs of AR-97Q mice lack synaptophysin and phopsho-neurofilament H staining owing to denervation (arrowheads), and this phenomenon was further enhanced by *Hsf-1* depletion. (**l**) The frequency of denervation at NMJ is significantly increased in heterozygous *Hsf-1*-knockout AR-97Q mice. (**m**) Immunohistochemistry for Gfap in the anterior horn of the spinal cord. (**n**) Quantitative analysis of anti-Gfap immunoreactivity. (**o**) Immunoblotting for Gfap in the spinal cord of AR-97Q and *Hsf-1*-knockout AR-97Q mice (13 weeks old). (**p**) Quantitative analysis of the signal intensity of the Gfap-immunoreactive bands. Unpaired *t*-test. More than 500 neurons from three brains were analysed in each group (**e**–**h**), $n=3$ (**j**). Unpaired *t*-test. $n=3$ for each group (**l**), $n=5$ (**n**). Error bars indicate s.e.m. (**e**–**h**,**j**,**l**,**n**,**p**). Scale bars, 50 μm (**a**–**d**,**k**,**m**).

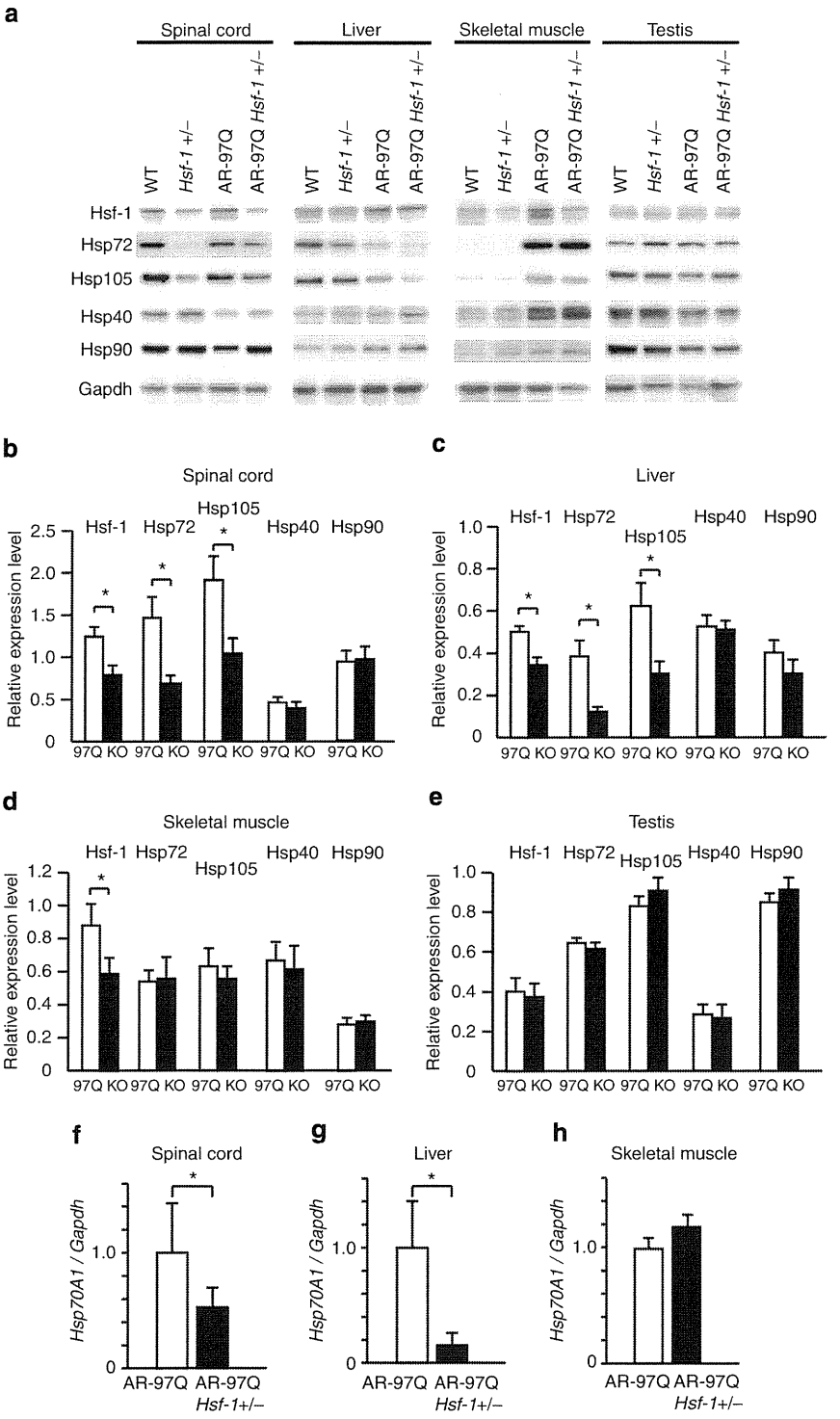

Figure 6 | Expression levels of Hsps in tissues from *Hsf-1*-knockout AR-97Q mice. (**a**) Immunoblotting for Hsf-1, Hsp72, Hsp105, Hsp40 and Hsp90 in wild-type, *Hsf-1*-knockout wild-type, AR-97Q and Hsf-1-knockout AR-97Q mice (13 weeks old). (**b**–**e**) Quantitative analysis using densitometry revealed that the expression levels of Hsp72 in the spinal cord (**b**) and liver (**c**) were downregulated in heterozygous *Hsf-1*-knockout AR-97Q mice compared with AR-97Q mice (13 weeks old). No significant alterations in the signal intensity of the Hsp-immunoreactive bands were observed in skeletal muscle (**d**) or testis (**e**). Data are shown as the ratio of the intensity of each molecule to Gapdh. (**f**–**h**) Quantification of *Hsp70A1* mRNA levels using RT-PCR in the spinal cord (**f**), liver (**g**) and skeletal muscle (**h**). $^*P<0.05$ by unpaired *t*-test ($n=7$) (**b**–**e**), and ($n=3$) (**f**–**h**). The inter-group differences were not significant, unless otherwise mentioned. Error bars indicate s.e.m. (**b**–**h**).

The results of the present study also revealed the tissue-specific regulation of Hsps by Hsf-1. Despite downregulation of Hsps in spinal cord and liver, *Hsf-1* depletion had no effect on the expression of Hsps in the testis of AR-97Q mice, presumably owing to an incomplete reduction of Hsf-1 protein levels. Furthermore, the inactivation of Hsf-1 did not decrease the expression levels of Hsps or enhance the accumulation of pathogenic AR in the skeletal muscle of SBMA mice, suggesting

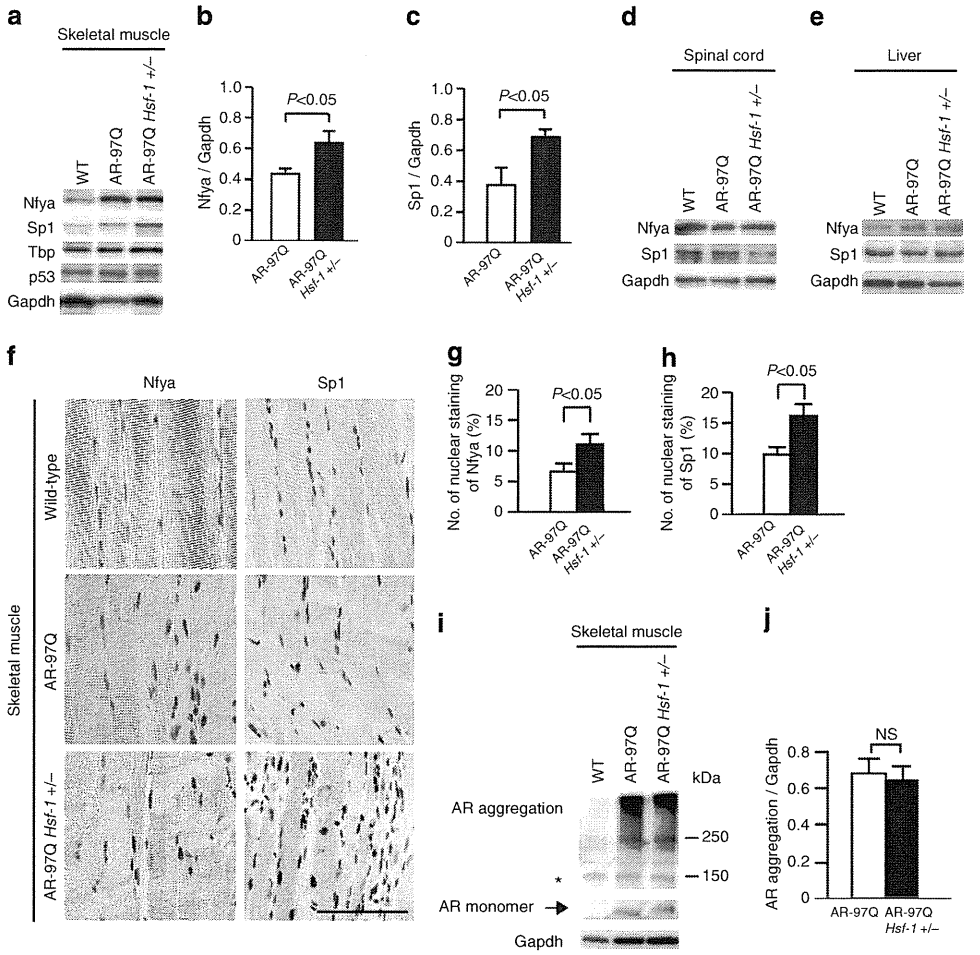

Figure 7 | Expression levels of Hsp70 inducers in skeletal muscle. (**a**) Immunoblotting for Nfya, Sp1, p53 and Tbp in wild-type, AR-97Q and heterozygous *Hsf-1*-knockout AR-97Q mice (13 weeks old). (**b**,**c**) Quantitative analysis using densitometry revealed that the expression levels of Nfya and Sp1 in skeletal muscle were upregulated in heterozygous *Hsf-1*-knockout AR-97Q mice compared with AR-97Q mice (13 weeks old). (**d**,**e**) Immunoblotting for Nfya and Sp1 in the spinal cord and liver in the mice of each group (13 weeks old). (**f**) Immunohistochemistry of skeletal muscle in wild-type, AR-97Q and *Hsf-1*-knockout AR-97Q mice using anti-Nfya and anti-Sp1 antibodies (13 weeks old). The nuclear uptake of Nfya and Sp1 was upregulated in AR-97Q mice compared with wild-type mice, and further intensified in heterozygous *Hsf-1*-knockout AR-97Q mice. (**g**,**h**) Quantification of immunohistochemistry with Nfya and Sp1 in the skeletal muscle of heterozygous *Hsf-1*-knockout AR-97Q mice compared with AR-97Q mice (13 weeks old). (**i**) Immunoblotting for AR in wild-type, AR-97Q and *Hsf-1*-knockout AR-97Q mice (13 weeks old). *Nonspecific bands. Quantitative analysis of immunoblots using densitometry indicated that the expression levels of abnormal AR aggregations in the skeletal muscle had no significant change in heterozygous *Hsf-1*-knockout AR-97Q mice compared with AR-97Q mice (**j**). Unpaired *t*-test ($n = 3$). Error bars, s.e.m. (**b**,**c**,**g**,**h**,**j**). Scale bars, 50 μm (**f**). NS, not significant.

that molecules other than Hsf-1 may maintain the expression of Hsps. The upregulation of Nfya and Sp1 in the skeletal muscle of the heterozygous *Hsf-1*-knockout AR-97Q mice appears to compensate for the deleterious effects of *Hsf-1* depletion on the transcriptional regulation of Hsp70, given that these molecules are capable of inducing the expression of Hsps in certain circumstances[36,37,48]. In contrast, this compensatory mechanism does not function in the spinal cord, providing another molecular basis for the vulnerability of motor neurons in SBMA. In support of our findings, a cell-specific compensatory mechanism was shown to influence the selectivity of pathogenic lesions in a mouse model of HD[49]. As Hsf-1 is known to have diverse functions in healthy and disease conditions, such as longevity and inflammation[50,51], further study is needed to thoroughly understand the entire effects of *Hsf-1* depletion on the pathogenesis of neurodegenerative diseases. From the therapeutic point of view, the manipulation of tissue-specific regulatory systems of Hsps may be a key strategy to combat the toxicity of polyglutamine-expanded proteins.

Methods

Animals. AR-97Q mice were generated by using the pCAGGS vector and maintained as described previously[25,40]. The AR-97Q and heterozygous *Hsf-1*-knockout AR-97Q mice, as well as the heterozygous *Hsf-1*-knockout wild-type and wild-type mice used in the experiments described here, were derived by crossing heterozygous *Hsf-1*-knockout C57BL6 mice with AR-97Q mice[33]. All of the experiments were performed on male mice derived from the cross described above. The mice were genotyped by PCR on tail DNA[25,33].

Behavioural analysis. All of the tests were performed weekly, and the data were analysed prospectively as described in Supplementary Methods. All of the animal experiments were performed in accordance with the National Institutes of Health Guide for the Care and Use of Laboratory Animals and under the approval of the Nagoya University Animal Experiment Committee.

Autopsy specimens. Autopsy specimens of the CNS, including the spinal cord, cerebrum and cerebellum, and non-neuronal tissues, such as the pancreas, spleen and colon, were obtained from three genetically confirmed SBMA patients (52, 77 and 78 years old) and three control subjects (58, 64 and 70 years old). Representative sections are shown in Supplementary Fig. S2. The collection of tissues and their use for this study were approved by the Ethics Committee of Nagoya University Graduate School of Medicine.

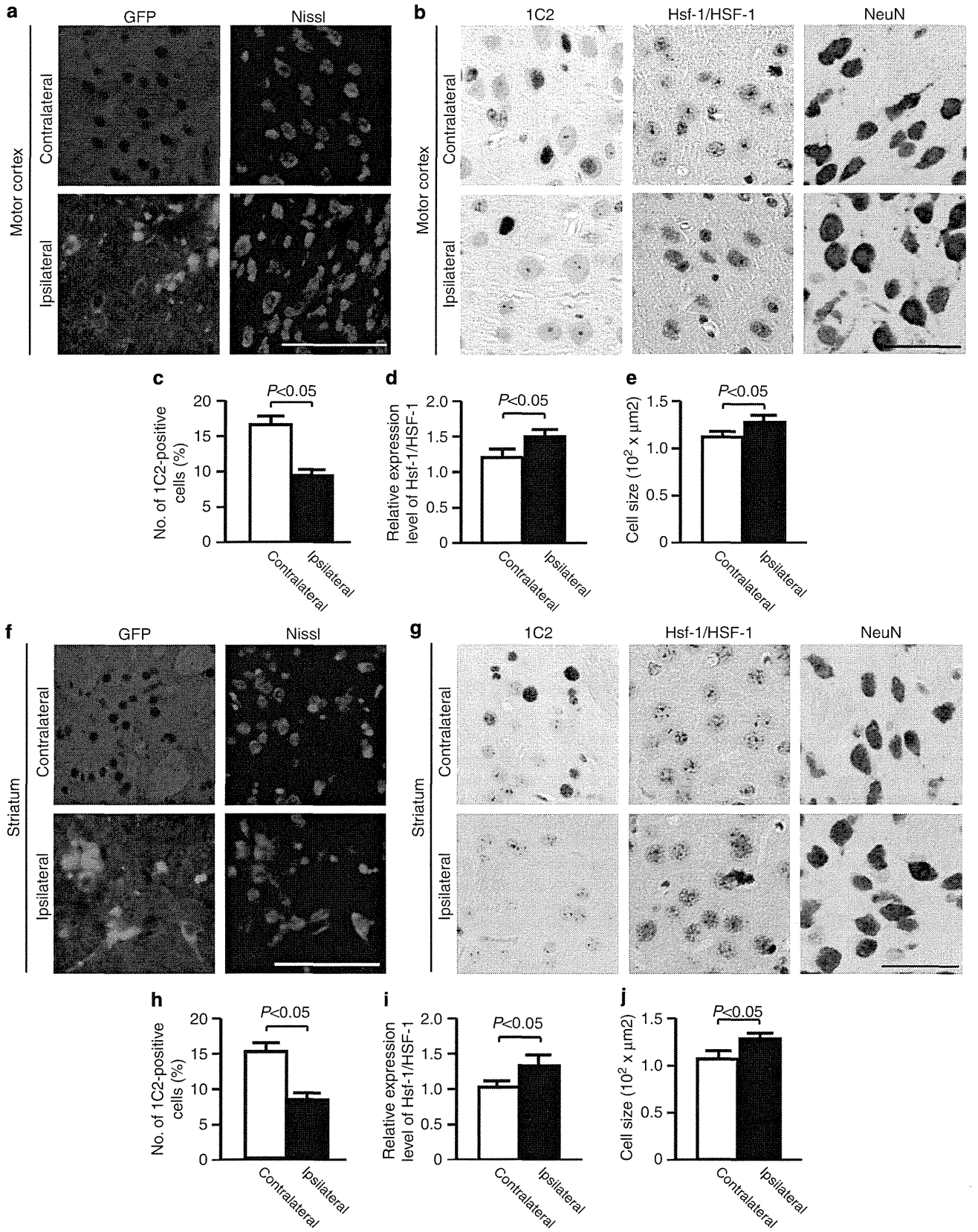

Figure 8 | HSF-1 alleviates neuronal atrophy in the motor cortex and striatum of AR-97Q mice. (**a**,**f**) Expression of transgenes in the motor cortex (**a**) and striatum (**f**) of the AR-97Q mice 3 weeks after injection. (**b**,**g**) Immunohistochemistry for Hsf-1/HSF-1, 1C2 and NeuN in the motor cortex and striatum of AR-97Q mice. The regions injected with lentiviral vector expressing hHSF-1 were compared with the contralateral side of the same mouse (13 weeks old). (**c**–**e**, **h**–**j**) Quantitative analyses of the frequency of 1C2-positive cells (**c**,**h**), relative expression level of Hsf-1/HSF-1 (**d**,**i**) and cell size of neuronal cells (**e**,**j**) confirmed the neuroprotection by the lentiviral delivery of HSF-1 into the motor cortex and striatum of AR-97Q mice. Unpaired *t*-test. More than 300 neurons from three brains were analysed in each group (**c**–**e**,**h**–**j**). Error bars indicate s.e.m. (**c**–**e**,**h**–**j**). Scale bars, 100 µm (**a**,**f**) and 50 µm (**b**,**g**).

Immunoblotting. Mouse tissues were homogenized in buffer containing 50 mM Tris–HCl (pH 8.0), 150 mM NaCl, 1% Nonidet P-40, 0.5% deoxycholate, 0.1% SDS and 1 mM 2-mercaptoethanol with 1 mM phenylmethylsulphonyl fluoride and 6 μg ml^{-1} aprotinin and then centrifuged at 2,500 *g* for 15 min. Equal amounts of protein were separated by 5–20% SDS/PAGE and transferred to Hybond-P membranes (GE Healthcare, Piscataway, NJ, USA). The primary antibodies and their dilutions were as follows: AR (N20, 1:1,000; Santa Cruz Biotechnology, Santa Cruz, CA, USA), Hsp72 (1:1,000; Stressgen Biotechnologies, Victoria, Canada), Hsp40 (1:5,000; Stressgen), Hsp90 (1:1,000; Stressgen), Hsp105 (1:250; Novocastra Laboratories, Newcastle, UK), Hsf-1 (1:5,000; Stressgen), ChAT (1:1,000; Millipore, Billerica, MA, USA), NF-YA (G-2, 1:500; Santa Cruz Biotechnology), SP1 (PEP2, 1:2,000; Santa Cruz Biotechnology), TBP (N-12, 1:500; Santa Cruz Biotechnology) and p53 (DO-1, 1:500, Santa Cruz Biotechnology). Primary antibody binding was probed with horseradish peroxidase-conjugated secondary antibodies at a dilution of 1:5,000, and bands were detected by using an immunoreaction-enhancing solution (Can Get Signal; Toyobo, Osaka, Japan) and enhanced chemiluminescence (ECL Plus; GE Healthcare). An LAS-3000 imaging system (Fujifilm, Tokyo, Japan) was used to produce digital images. The signal intensities of these independent blots were quantified using IMAGE GAUGE software version 4.22 (Fuji) and expressed in arbitrary units. The membranes were reprobed with an anti-GAPDH (1:5,000; Santa Cruz Biotechnology) antibody for normalization.

Histology and immunohistochemistry. Mice deeply anesthetized with pentobarbital were perfused with 4% paraformaldehyde fixative in phosphate buffer (pH 7.4). The tissues were dissected, post-fixed in 10% phosphate-buffered formalin and processed for paraffin embedding. Sections to be stained with an anti-polyglutamine antibody (1C2) were treated with formic acid for 5 min at room temperature; those to be incubated with an anti-HSF-1 antibody were boiled in 10 mM citrate buffer for 15 min. The primary antibodies and their dilutions were as follows: polyglutamine (1:20,000; Millipore), Hsp72 (1:500; Stressgen), anti-HSF-1 (1:5,000; Stressgen), ChAT (1:1,000; Millipore), GFAP (1:2,000; Epitomics, Burlingame, CA, USA), NF-YA (H-209, 1:500; Santa Cruz Biotechnology), SP1 (PEP2, 1:2,000; Santa Cruz Biotechnology), TBP (N-12, 1:500; Santa Cruz Biotechnology), and p53 (DO-1, 1:500; Santa Cruz Biotechnology). Primary antibody binding was probed with a secondary antibody labelled with a polymer as part of the Envision + system containing horseradish peroxidase (Dako Cytomation, Gostrup, Denmark).

Lentiviral vector construct preparation. The cds portion of human *HSF-1* complementary DNA[33] was subcloned into the pEGFP expression vector through *Age1* and *Xho1* restriction sites. *hHSF-1-GFP* was inserted into the pENTR/D/TOPO vector (Invitrogen, Carlsbad, CA) and transferred into the pLenti CMV Neo DEST #2 (705-1) vector, a gift from Dr Eric Campeau (Resverlogix Corp.), using the Gateway system (Invitrogen).

Viral production. Lentivirus was prepared following Campeu's protocol[52]. Briefly, lentiviral particles were produced in HEK293FT cells by transfection using Lipofectamine 2000 (Invitrogen). The lentiviral-containing supernatant was collected 48 h after transfection, and concentrated by ultracentrifugation. The viral titre was measured using Lenti-X qRT-PCR Titration Kit (Clontech, Mountain View, CA).

Injection procedures. Recombinant lentiviral vector expressing hHSF1-GFP or GFP alone (6.7×10^8 copies per μl) was stereotaxically injected into the right motor cortex and striatum (1 μl per 10 min) of 8-week-old AR-97Q mice deeply anethetized with pentobarbital, using a Hamilton syringe (Hamilton, Reno, NV, USA) and a microinjection cannula (Eicom, Kyoto, Japan) as described in Supplementary Method.

Quantitative analysis of immunohistochemistry. To assess 1C2-positive cells, we prepared at least 100 consecutive 6-μm-thick axial sections of the thoracic spinal cord, coronal sections of the cerebrum and cerebellum, and longitudinal sections of skeletal muscle, and immunostained every tenth section with an anti-1C2 antibody. The number of 1C2-positive cells was counted in all of the motor neurons within the anterior horn of the ten axial sections from the thoracic spinal cord and more than 500 neurons in five randomly selected X400 microscopic fields of the ten sections in each region from the cerebrum and cerebellum of each group of mice ($n = 3$) under a light microscope (Bx51; Olympus, Tokyo, Japan). The frequency of 1C2-positive cells was expressed as the number per 100 neurons. For the assessment of 1C2-positive cells in skeletal muscle, the number of 1C2-positive cells was calculated for more than 500 fibres in randomly selected areas of the ten axial sections and the results were expressed as the number per 100 muscle fibres. To measure the number of 1C2-positive cells in the liver and pituitary gland, more than 500 cells in randomly selected areas of the ten axial sections were investigated and the results were expressed as the number per 100 cells. For the quantification of the expression levels of Hsf-1, Nfya, p53, Tbp and Sp1, we performed immunohistochemistry on every 20th section from the 100 consecutive sections. We measured the intensity of nuclear immunoreactivity for each molecule in the anterior horn of the five axial sections from the thoracic spinal cord and more than 500 cells in five randomly selected X400 microscopic fields of the five sections from the cerebral motor and visual cortex, striatum, and cerebellar Purkinje and granule cells from each group of mice ($n = 3$) using an image analyser (WinROOF; Mitani Corporation, Tokyo, Japan). We also measured the intensity of immunoreactivity in the ependymal cells of each section as a standard control, and calculated the signal intensity ratio using this control. To quantify the cell size of motor neurons and the region of anti-GFAP immunoreactivity in the spinal anterior horn, we analysed every tenth section of the 50 consecutive 6-μm-thick axial sections from the thoracic spinal cord using an image analyser (WinROOF). For the purposes of calculating the cell size of hepatocytes, cerebellar Purkinje cells, striatal neurons and cerebral cortex neurons, more than 500 neurons and 1000 hepatocytes in randomly selected areas were examined using an image analyser (WinROOF). To analyse the pathological change in the brain with the lentivirus injection, we prepared consecutive 3-μm-thick coronal sections of the cerebrum and immunostained every five sections with 1C2 and anti-Hsf-1 antibodies. The number of 1C2-positive cells was counted in more than 300 neurons in a X400 microscopic fields around the lentivirus injection site from the five sections under a light microscope (Bx51; Olympus, Tokyo, Japan). We measured the intensity of nuclear immunoreactivity for Hsf-1 in more than 300 cells in X400 microscopic fields using an image analyser (WinROOF).

NMJ staining. 30 μm-thick frozen longitudinal sections of the gastrocnemius muscle were incubated overnight with α-bungarotoxin conjugated with biotinXX (1:80, Invitrogen), anti-phosphorylated NF-H mouse monoclonal antibody (SMI31, 1:100, Covance) and anti-synaptophysin rabbit polyclonal antibody (1:100, Cell Signaling Technologies). After washing, sections were incubated with goat anti-rabbit and anti-mouse IgG conjugated with Alexa 488 (1:1,000 for each, Invitrogen) and streptavidin conjugated with Alexa 564 (1:1,000, Invitrogen) and mounted with Prolong gold (Invitrogen). The stained sections were imaged with an upright microscope (Axio Imager M1, Zeiss). More than 50 NMJs from AR-97Q and heterozygous Hsf-1-knockout AR-97Q mice (13 weeks old) were analysed ($n = 3$).

Quantitative real-time reverse transcriptase PCR (RT-PCR). The mRNA levels of *Hsp70A1* were analysed by real-time RT-PCR as described previously[41]. Detailed methods are described in Supplementary Methods.

Statistical analysis. We analysed the data by using the unpaired Student's *t*-test for two group comparisons, and the Kaplan–Meier and log-rank tests for survival rate using STATVIEW software version 5 (Hulinks, Tokyo, Japan), and denoted *P*-values of 0.05 or less as statistically significant.

References

1. Morimoto, R. I. & Santoro, M. G. Stress-inducible responses and heat shock proteins: new pharmacologic targets for cytoprotection. *Nat. Biotechnol.* **16,** 833–838 (1998).
2. Hartl, F. U., Bracher, A. & Hayer-Hartl, M. Molecular chaperones in protein folding and proteostasis. *Nature* **475,** 324–332 (2011).
3. Wyttenbach, A. Role of heat shock proteins during polyglutamine neurodegeneration: mechanisms and hypothesis. *J. Mol. Neurosci.* **23,** 69–96 (2004).
4. Muchowski, P. J. & Wacker, J. L. Modulation of neurodegeneration by molecular chaperones. *Nat. Rev. Neurosci.* **6,** 11–22 (2005).
5. Hoshino, T. *et al.* Suppression of Alzheimer's disease-related phenotypes by expression of heat shock protein 70 in mice. *J. Neurosci.* **31,** 5225–5234 (2011).
6. Gifondorwa, D. J. *et al.* Exogenous delivery of heat shock protein 70 increases lifespan in a mouse model of amyotrophic lateral sclerosis. *J. Neurosci.* **27,** 13173–13180 (2007).
7. Wacker, J. L. *et al.* Hsp70 and Hsp40 attenuate formation of spherical and annular polyglutamine oligomers by partitioning monomer. *Nat. Struct. Mol. Biol.* **11,** 1215–1222 (2004).
8. Bailey, C. K., Andriola, I. F., Kampinga, H. H. & Merry, D. E. Molecular chaperones enhance the degradation of expanded polyglutamine repeat androgen receptor in a cellular model of spinal and bulbar muscular atrophy. *Hum. Mol. Genet.* **11,** 515–523 (2002).
9. Chan, H. Y. *et al.* Genetic modulation of polyglutamine toxicity by protein conjugation pathways in Drosophila. *Hum. Mol. Genet.* **11,** 2895–2904 (2002).
10. Adachi, H. *et al.* Heat shock protein 70 chaperone overexpression ameliorates phenotypes of the spinal and bulbar muscular atrophy transgenic mouse model by reducing nuclear-localized mutant androgen receptor protein. *J. Neurosci.* **23,** 2203–2211 (2003).
11. Katsuno, M. *et al.* Pharmacological induction of heat-shock proteins alleviates polyglutamine-mediated motor neuron disease. *Proc. Natl Acad. Sci. USA* **102,** 16801–16806 (2005).

12. Anckar, J. & Sistonen, L. Regulation of HSF1 function in the heat stress response: implications in aging and disease. *Ann. Rev. Biochem.* **80,** 1089–1115 (2011).
13. Holmberg, M. *et al.* Spinocerebellar ataxia type 7 (SCA7): a neurodegenerative disorder with neuronal intranuclear inclusions. *Hum. Mol. Genet.* **7,** 913–918 (1998).
14. Yamada, M. *et al.* Polyglutamine disease: recent advances in the neuropathology of dentatorubal-pallidoluysian atrophy. *Neuropathology* **26,** 346–351 (2006).
15. Tanaka, M. *et al.* Intra- and intermolecular beta-pleated sheet formation in glutamine-repeat inserted myoglobin as a model for polyglutamine diseases. *J. Biol. Chem.* **276,** 45470–45475 (2001).
16. Okazawa, H. *et al.* Interaction between mutant ataxin-1 and PQBP-1 affects transcription and cell death. *Neuron* **34,** 701–713 (2002).
17. Subramaniam, S., Sixt, K. M., Barrow, R. & Snyder, S. H. Rhes, a striatal specific protein, mediates mutant-huntingtin cytotoxicity. *Science* **324,** 1327–1330 (2009).
18. Tagawa, K. *et al.* The induction levels of heat shock protein 70 differentiate the vulnerabilities to mutant huntingtin among neuronal subtypes. *J. Neurosci.* **27,** 868–880 (2007).
19. Yamanaka, T. *et al.* Mutant Huntingtin reduces HSP70 expression through the sequestration of NF-Y transcription factor. *EMBO J.* **27,** 827–839 (2008).
20. Adachi, H. *et al.* Widespread nuclear and cytoplasmic accumulation of mutant androgen receptor in SBMA patients. *Brain* **128,** 659–670 (2005).
21. Yamada, M. *et al.* Widespread occurrence of intranuclear atrophin-1 accumulation in the central nervous system neurons of patients with dentatorubral-pallidoluysian atrophy. *Ann. Neurol.* **49,** 14–23 (2001).
22. Nucifora, F. C. *et al.* Interference by huntingtin and atrophin-1 with cbp-mediated transcription leading to cellular toxicity. *Science* **291,** 2423–2428 (2001).
23. Minamiyama, M. *et al.* Sodium butyrate ameliorates phenotypic expression in a transgenic mouse model of spinal and bulbar muscular atrophy. *Hum. Mol. Genet.* **13,** 1183–1192 (2004).
24. Ranganathan, S. *et al.* Mitochondrial abnormalities in spinal and bulbar muscular atrophy. *Hum. Mol. Genet.* **18,** 27–42 (2009).
25. Katsuno, M. *et al.* Testosterone reduction prevents phenotypic expression in a transgenic mouse model of spinal and bulbar muscular atrophy. *Neuron* **35,** 843–854 (2002).
26. Takeyama, K. *et al.* Androgen-dependent neurodegeneration by polyglutamine-expanded human androgen receptor in *Drosophila*. *Neuron* **35,** 855–864 (2002).
27. Katsuno, M. *et al.* Leuprorelin rescues polyglutamine-dependent phenotypes in a transgenic mouse model of spinal and bulbar muscular atrophy. *Nat. Med.* **9,** 768–773 (2003).
28. Chevalier-Larsen, E. S. *et al.* Castration restores function and neurofilament alterations of aged symptomatic males in a transgenic mouse model of spinal and bulbar muscular atrophy. *J. Neurosci.* **24,** 4778–4786 (2004).
29. Kennedy, W. R., Alter, M. & Sung, J. H. Progressive proximal spinal and bulbar muscular atrophy of late onset. A sex-linked recessive trait. *Neurology* **18,** 671–680 (1968).
30. Sobue, G. *et al.* X-linked recessive bulbospinal neuronopathy. A clinicopathological study. *Brain* **112**(Part 1): 209–232 (1989).
31. Orr, H. T. & Zoghbi, H. Y. Trinucleotide repeat disorders. *Ann. Rev. Neurosci.* **30,** 575–621 (2007).
32. Doyu, M. *et al.* Androgen receptor mRNA with increased size of tandem CAG repeat is widely expressed in the neuronal and nonneuronal tissues of X-linked recessive bulbospinal neuronopathy. *J. Neurol. Sci.* **127,** 43–47 (1994).
33. Hayashida, N. *et al.* Heat shock factor 1 ameliorates proteotoxicity in cooperation with the transcription factor NFAT. *EMBO J.* **29,** 3459–3469 (2010).
34. Nagai, Y. *et al.* A toxic monomeric conformer of the polyglutamine protein. *Nat. Struct. Mol. Biol.* **14,** 332–340 (2007).
35. Mason, Jr P. B. & Lis, J. T. Cooperative and competitive protein interactions at the hsp70 promoter. *J. Biol. Chem.* **272,** 33227–33233 (1997).
36. Li, Q. *et al.* Xenopus NF-Y pre-sets chromatin to potentiate p300 and acetylation-responsive transcription from the Xenopus hsp70 promoter *in vivo*. *EMBO J.* **17,** 6300–6315 (1998).
37. Pore, N. *et al.* Sp1 is involved in Akt-mediated induction of VEGF expression through an HIF-1-independent mechanism. *Mol. Biol. Cell* **15,** 4841–4853 (2004).
38. Fujimoto, M. *et al.* Active HSF1 significantly suppresses polyglutamine aggregate formation in cellular and mouse models. *J. Biol. Chem.* **280,** 34908–34916 (2005).
39. Kobayashi, Y. *et al.* Chaperones Hsp70 and Hsp40 suppress aggregate formation and apoptosis in cultured neuronal cells expressing truncated androgen receptor protein with expanded polyglutamine tract. *J. Biol. Chem.* **275,** 8772–8778 (2000).
40. Adachi, H. *et al.* CHIP overexpression reduces mutant androgen receptor protein and ameliorates phenotypes of the spinal and bulbar muscular atrophy transgenic mouse model. *J. Neurosci.* **27,** 5115–5126 (2007).
41. Waza, M. *et al.* 17-AAG, an Hsp90 inhibitor, ameliorates polyglutamine-mediated motor neuron degeneration. *Nat. Med.* **11,** 1088–1095 (2005).
42. La Spada, A. R. *et al.* Androgen receptor gene mutations in X-linked spinal and bulbar muscular atrophy. *Nature* **352,** 77–79 (1991).
43. Nagai, Y., Fujikake, N., Popiel, H. A. & Wada, K. Induction of molecular chaperones as therapeutic strategy for the polyglutamine diseases. *Curr. Pharm. Biotechnol.* **11,** 188–197 (2010).
44. Rimoldi, M., Servadio, A. & Zimarino, V. Analysis of heat shock transcription factor for suppression of polyglutamine toxicity. *Brain Res. Bull.* **56,** 353–362 (2001).
45. Okabe, M. *et al.* 'Green mice' as a source of ubiquitous green cells. *FEBS Lett.* **407,** 313–319 (1997).
46. Mieulet, V. *et al.* S6 kinase inactivation impairs growth and translational target phosphorylation in muscle cells maintaining proper regulation of protein turnover. *Am. J. Physiol. Cell Physiol.* **293,** C712–C722 (2007).
47. Tokui, K. *et al.* 17-DMAG ameliorates polyglutamine-mediated motor neuron degeneration through well-preserved proteasome function in an SBMA model mouse. *Hum. Mol. Genet.* **18,** 898–910 (2009).
48. Marinova, Z. *et al.* Valproic acid induces functional heat-shock protein 70 via Class II histone deacetylase inhibition in cortical neurons: a potential role of Sp1 acetylation. *J. Neurochem.* **111,** 976–987 (2009).
49. Yamanaka, T. *et al.* Mutant huntingtin fragment selectively suppresses Brn-2 POU domain transcription factor to mediate hypothalamic cell dysfunction. *Hum. Mol. Genet.* **19,** 2099–2112 (2010).
50. Hsu, A. L. *et al.* Regulation of aging and age-related disease by DAF-16 and heat shock factor. *Science* **300,** 1142–1145 (2003).
51. Inouye, S. *et al.* Heat shock transcription factor 1 opens chromatin structure of interleukin-6 promoter to facilitate binding of an activator or a repressor. *J. Biol. Chem.* **282,** 33210–33217 (2007).
52. Campeau, E. *et al.* A versatile viral system for expression and depletion of proteins in mammalian cells. *PLoS One* **4,** e6529 (2009).

Acknowledgements

This work was supported by a Global COE Program, MEXT, Japan; MEXT/JSPS KAKENHI Grant Number 21229011, 21689024, 22110005 and 23390230; Health Labour Sciences Research Grants, MHLW, Japan; CREST, JST; and a grant from Kennedy Disease Association.

Author contributions

Project planning was performed by N.K., M.K., A.N. and G.S.; experimental work by N.K., M.K., H.A., M.M., H.D., S.M., Y.M., M.I., G.T., H.N., S.I., Y.F., H.W. and F.T.; data analysis by N.K., M.K. and G.S.; composition of the first draft of the manuscript by N.K. and M.K.; and manuscript layout by A.N. and G.S.

Additional information

Supplementary Information accompanies this paper at http://www.nature.com/naturecommunications

Competing financial interests: The authors declare no competing financial interests.

Reprints and permission information is available online at http://npg.nature.com/reprintsandpermissions/

How to cite this article: Kondo, N. *et al.* Heat shock factor-1 influences pathological lesion distribution of polyglutamine-induced neurodegeneration. *Nat. Commun.* 4:1405 doi: 10.1038/ncomms2417 (2013).